Structural studies on the stalk region of the axonemal and cytoplasmic dynein heavy chain

(軸糸および細胞質ダイニン重鎖にあるストーク領域の構造研究)

Doctoral thesis

by

Seolmin Ko

Submitted to Graduate School of Science

Osaka University

Japan

August 2023

Table of contents

Acknowledgement·····**1**

I. Abstract·····**3**

II. List of abbreviations·····**5**

III. Background information·····**7**

1. Motor proteins·····7

2. Cytoskeleton·····8

Chapter 1. Introduction·····**9**

1.1 Dynein motor protein·····9

1.2 Research plan·····18

Chapter 2. Human inner-arm dynein heavy chain d stalk and MTBD·····**19**

2.1 Introduction·····19

2.2 Materials and methods·····21

2.3 Results·····25

2.4 Discussion·····43

Chapter 3. Triple complex of the SRS fused-human dynein and the porcine tubulin dimer with adaptor protein·····**47**

3.1 Introduction·····47

3.2 Materials and methods·····49

3.2.1 SRS-fused human dynein·····49

3.2.2 Porcine tubulin·····53

3.2.3 D1 designed ankyrin repeat protein (DARPin) ·····55

3.2.4 Triple complex·····57

3.3 Results·····58
3.3.1 SRS-fused human dynein·····58
3.3.2 Triple complex·····69
3.4 Discussion·····77

Chapter 4. Conclusion·····79

IV. References·····81

V. List of publication·····88

Acknowledgement

I would like to express my heartfelt gratitude to everyone who has supported me throughout my journey in completing this PhD program. First and foremost, I am deeply grateful to my supervisor, Professor Genji Kurisu, for accepting me into his lab and providing me with invaluable guidance and advice. Despite his busy schedule, he always made time for personal discussions, which greatly contributed to my growth as a researcher. I consider myself fortunate to have had such a dedicated and inspiring mentor.

I would like to extend my sincere appreciation to my wife, Sieun Lee, for her unwavering support. Her belief in me and her encouragement during the challenging times of my experiments and thesis writing were instrumental in my perseverance. Without her, completing this PhD program would have been much more difficult, and I am truly grateful for her presence in my life. I would also like to thank my parents, who have always been concerned and supportive of me.

I would also like to thank Prof. Hideaki Tanaka for his invaluable assistance whenever I faced experimental difficulties in the dynein project. His expertise and guidance were crucial in overcoming obstacles and making progress. Additionally, I am grateful to Prof. Jian Yu for his tremendous support in structural analysis, as well as to Prof. Young-ho Lee and Dr. Yuxi Lin from KBSI for their assistance in characterization experiments. I am also thankful to Prof. Bekker Gert-Jan for his help with MD simulation.

Lastly, I want to express my appreciation to my friends Dr. Orkun Çoruh and Jennifer Neumann for their companionship and support during the initial years of my PhD program. Their friendship made my time in Japan more enjoyable and helped me navigate the challenges of living in a new country.

To all the individuals mentioned above and to those whose names might not be mentioned but who have played a part in my academic journey, I offer my sincerest thanks. Your support, encouragement, and guidance have been invaluable, and I am truly grateful for the opportunity to have worked with such remarkable individuals.

Seolmin Ko

August, 2023

Abstract

Dynein motors, including axonemal and cytoplasmic dyneins, are an ATP-dependent microtubular motor protein responsible for various biological processes and their dysfunction can lead to various diseases. Despite its biological importance, structure-based dynein motor mechanisms remain unclear. In this study, I focused on two specific aspects: the structural characterization of axonemal dynein stalk and the interaction between cytoplasmic dynein microtubule-binding domain (MTBD) and microtubules.

For axonemal dynein, the X-ray crystal structure of human inner-arm dynein-d (DNAH1) with a long coiled-coil stalk region was successfully determined as the first high resolution structure of axonemal dynein stalk, enabling for a direct comparison with cytoplasmic and outer-arm dynein structures. The structural comparison revealed distinctive characteristics in helical interaction, domain arrangement and flap motif extension. Notably, additional analysis of knobs-into-hole packing of long coiled coil and relative domain arrangement suggested a type-specific packing tightness and interacting pattern. Based on these findings, a novel and isoform-specific "spike shoe model" was proposed to elucidate the role of the uniquely extended flap motif in axonemal dynein. These findings provide valuable insights into the underlying mechanism of axonemal dynein activity. Moreover, the first atomic structure of DNAH1 could be further used for a representative example for future high-resolution axonemal inner-arm dynein complex studies.

Regarding cytoplasmic dynein, I aimed to investigate the structural details of the MTBD and its interaction with microtubules. Previous attempts were limited by low-resolution structures or proteolysis of the MTBD during crystallization. To overcome these challenges, I developed a new construct, modified SRS-dynein fusion protein with α registry, fused with seryl tRNA-synthetase (SRS), to stabilize its coiled coil registry to “alpha” with high binding

affinity to microtubule. Additionally, I utilized the porcine tubulin and D1 DARPin protein to form a triple complex of SRS-dynein, D1 DARPin, and the porcine tubulin dimer for crystallization. Although I encountered difficulties with protein stability, I successfully obtained both the triple complexed proteins and modified SRS-dynein crystals in the desired form. Finally, I propose using she1 in future strategies to improve protein stability and gain a better understanding of the dynein-tubulin interactions.

Overall, this study contributes to our understanding of axonemal and cytoplasmic dynein motors by providing new insights into their structural characteristics and how they interact with microtubules.

List of abbreviations

AAA^+	ATPases associated with diverse cellular activities
ATP	Adenosine triphosphate
CC	Coiled coil
CV	Column volumes
DARPin	Designed ankyrin repeat protein
DNAH1	Human inner-arm dynein-d
DNAH1s	Human inner-arm dynein-d stalk
DTT	Dithiothreitol
EM	Electron microscopy
GTP	Guanosine triphosphate
HC	Heavy chain
IAD	Inner-arm dynein
IC	Intermediate chain
IMAC	Immobilized metal affinity chromatography
IPTG	Isopropyl β-D-1-thiogalactopyranoside
KIH	Knobs-into-holes
LB	Luria-Bertani
LC	Light chain
LIC	Light-intermediate chain
MR	Molecular replacement
MTBD	Microtubule-binding domain
MWCO	Molecular weight cut-off
NMR	Nuclear magnetic resonance

OAD	Outer-arm dynein
OD_{600}	Optical density at 600 nm
PCA	Principal Component Analysis
PCD	Primary ciliary dyskinesia
PDB	Protein Data Bank
PEG	Polyethylene glycol
rpm	rotations per minute
SAD	Single-wavelength anomalous dispersion
SDS-PAGE	Sodium dodecyl sulfate-polyacrylamide gel electrophoresis
SeMet	L-selenomethionine
SPring-8	Super Photon Ring-8 GeV
SRS	Seryl-tRNA synthetase
Tris	Tris (hydroxymethyl) aminomethane
V_M	Matthews coefficient

Background information

Cells are the fundamental units of life, and their proper functioning is critical for the survival of all organisms. One key aspect of cell function is the ability to move, which relies on the coordinated action of motor proteins and the cytoskeleton. Motor proteins utilize ATP hydrolysis to generate force and movement along cytoskeletal filaments, while the cytoskeleton provides structural support and contributes to essential cellular processes such as division, migration, and intracellular transport[1,2]. In the following sections, I will explore detailed information about motor proteins and the cytoskeleton, followed by an outline of my PhD research plan of the dynein project.

1. Motor Proteins

Motor proteins are a diverse class of molecular motors that play crucial roles in cell movement, intracellular transport, and various cellular processes. These proteins convert the chemical energy derived from ATP hydrolysis into mechanical work, enabling them to move along cytoskeletal filaments. There are three major types of motor proteins: myosin, kinesin, and dynein[3].

Myosin, an actin-based motor protein, generates the force required for muscle contraction. Kinesin, a microtubule-based motor protein, moves towards the plus end of microtubules and is involved in intracellular transport, mitosis, and meiosis. Dynein, on the other hand, is a minus-end-directed microtubule motor protein critical for intracellular transport, cilia and flagella movement, and nuclear migration[3–5].

2. Cytoskeleton

The cytoskeleton is a complex and dynamic network of protein filaments that maintains the structural integrity of cells and orchestrates essential cellular processes, including division, migration, and intracellular transportation. It consists of three major types of filaments: microtubules, intermediate filaments, and actin filaments[6–8].

Microtubules are long, hollow tubes composed of tubulin proteins and play critical roles in cell division, intracellular transportation, and the movement of cellular appendages such as cilia and flagella[6]. Intermediate filaments, on the other hand, consist of fibrous proteins that confer mechanical stability to the cells, particularly in tissues subjected to mechanical stress, such as skin and hair[7]. Actin filaments, also known as microfilaments, are thin and flexible filaments composed of actin proteins. They are integral to cell movement and muscle contraction, generating force and facilitating cellular motility[8].

The cytoskeleton, together with motor proteins, forms an intricate system that allows cells to move, maintain their shape, and perform essential functions. Understanding the mechanisms and interactions of these components provides insights into the fundamental function underlying cellular biology.

Chapter 1

Introduction

1.1 Dynein motor protein

Cytoplasmic and axonemal dynein

Dyneins are essential microtubule-based molecular motors that play a vital role in a wide range of biological processes. These motors form large complexes, exceeding 1 MDa in size, and consist of various subunits, including the heavy chain (HC), intermediate chain (IC), light-intermediate chain (LIC), and light chain (LC)[9] **(Figure 1)**. Broadly categorized into two groups, cytoplasmic dynein and axonemal dynein, each type serves distinct physiological functions.

Cytoplasmic dynein primarily functions in intracellular transport and cell mitosis[10,11]. It facilitates the movement of organelles, vesicles, and other cargoes along microtubules towards the minus end. This motor protein is crucial for maintaining cellular organization, ensuring the proper distribution of cellular components, and enabling vital processes such as cell division.

On the other hand, axonemal dynein plays a key role in generating the propulsive force necessary for ciliary and flagellar beating[12,13]. The axoneme, the structural backbone of cilia and flagella, exhibits a characteristic 9+2 arrangement, composed of 9 doublet microtubules surrounding 2 central microtubules[14] **(Figure 2)**. Axonemal dyneins are regularly arranged within the axoneme and can be further classified into two sub-groups based on their location:

Outer-arm dynein (OAD), situated on the outer side of the axoneme, and Inner-arm dynein (IAD), positioned on the inner side[13].

Dysfunctions in dynein motor proteins have been associated with a variety of diseases. Defects in cytoplasmic dynein function have been linked to neurodegenerative disorders, where impaired intracellular transport contributes to the pathogenesis[15]. Abnormalities in axonemal dynein have been thought to be associated with ciliary dysfunctions and conditions such as primary ciliary dyskinesia (PCD)[16], which manifest as impaired ciliary movement and lead to various respiratory and reproductive system complications.

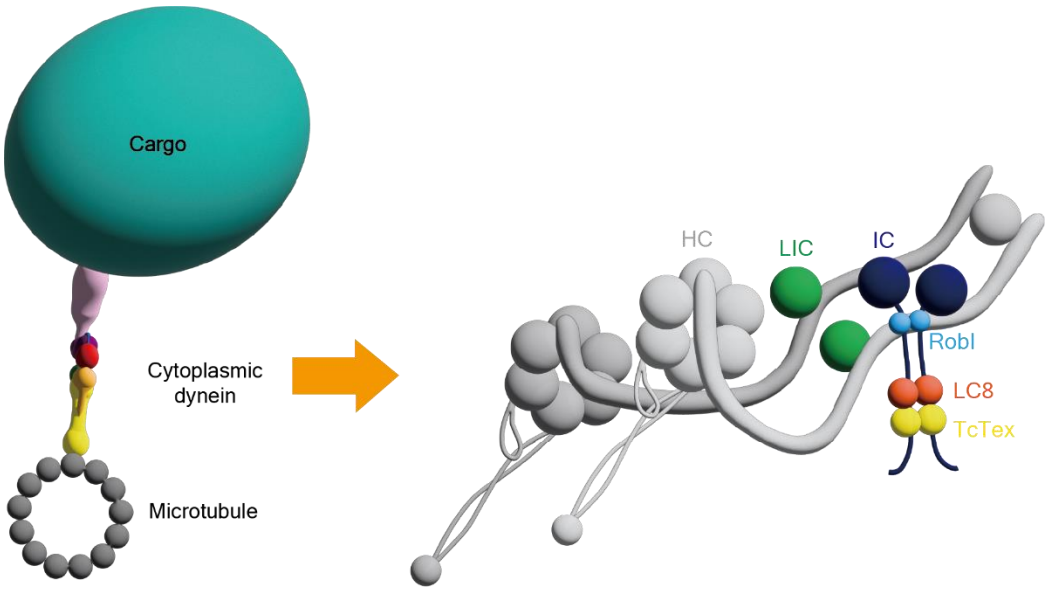

Figure 1. Overall structure of cytoplasmic dynein

Schematic diagram of the cytoplasmic dynein complex modified from Toda *et al.*, 2018[17]. (Left: Front view) Cytoplasmic dynein heavy chain highlighted in rainbow color. Cellular cargo and microtubule colored in teal and dark grey, respectively. (Right: Side view) Heavy chain (HC) represented in grey, while light-intermediate chain (LIC) is shown in green, intermediate chain (IC) in dark navy, Robl in cyan, LC8 in orange, and TcTex in yellow.

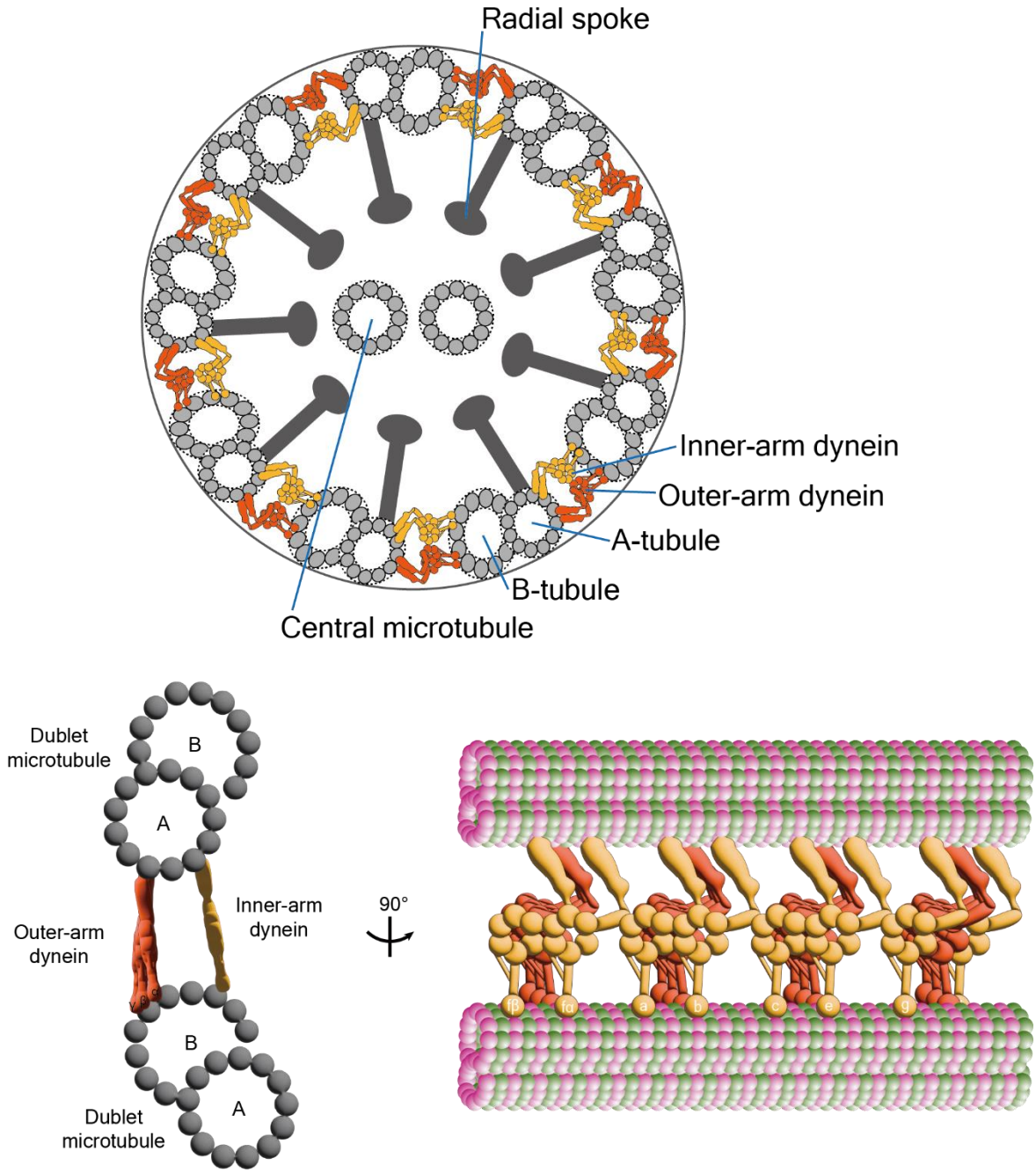

Figure 2. Overall architecture of axonemal dynein

Schematic illustration of axonemal dynein within the axoneme. Axonemal dyneins are categorized into two groups: inner-arm dyneins (colored in yellow) and outer-arm dyneins (colored in orange). These dyneins are permanently attached to the A-tubule of the outer doublet microtubule and make temporary contacts with the adjacent B-tubule.

Structure of dynein motor domain

As mentioned earlier, both axonemal and cytoplasmic dynein supramolecular complexes are composed of heavy, intermediate, light-intermediate, and light chains. Among them, the heavy chain forms the core region that performs major motor activities[18]. The dynein heavy chain consists of the N-terminal tail, which contains binding regions for other dynein subunits[19–21], and the motor domain composed of three functional units known as the linker, ATPases associated with diverse cellular activities (AAA^+) ring, and stalk **(Figure 3)**.

The linker domain is the mechanical element that generates the dynein power stroke. The AAA^+ ring has six conserved AAA^+ modules, three of which can bind or hydrolyze ADP or ATP to provide the driving force for motor activity. The stalk region consists of a long anti-parallel coiled coil that extends from the AAA4 module, and a small globular tip comprising the microtubule-binding domain (MTBD).

Additionally, the motor domain has another short coiled coil extending from the AAA5 module, named the strut/buttress. This coiled coil serves as a communication path between the AAA^+ ring and stalk during nucleotide-dependent conformational changes[3,5,20].

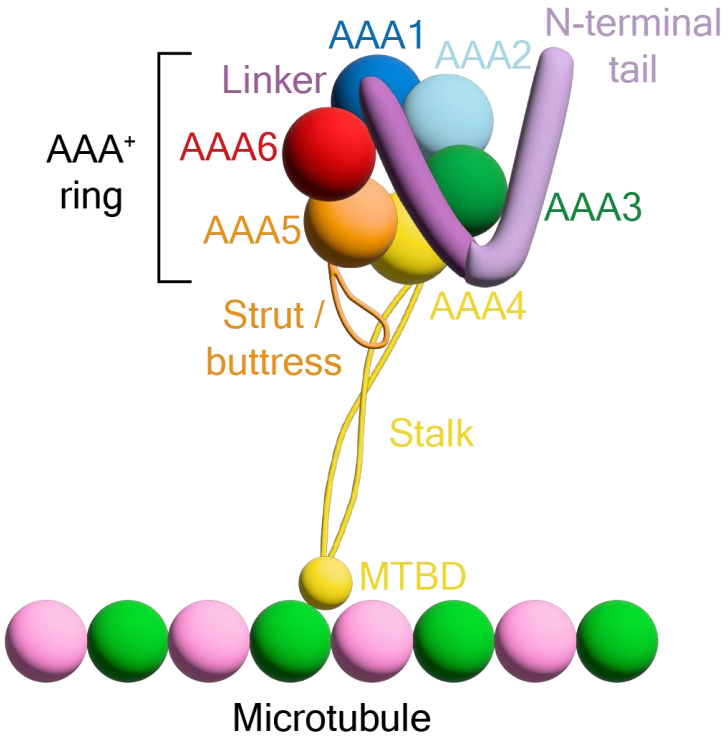

Figure 3. Overall structure of dynein motor domain

This schematic diagram depicts the dynein motor domain. The AAA^+ ring is color-coded in a rainbow scheme, representing different subdomains within the ring. The strut/buttress and the stalk coiled coil including MTBD are shown in the same color as that of basal AAA^+ subdomain, AAA4 module.

Dynein motor mechanism

Understanding the motor cycle of dynein has been the focus of numerous structural and biochemical studies, providing insights into the dynamic behavior of this molecular motor. Through these investigations, the current understanding of the dynein motor cycle has emerged, shedding light on the sequential steps involved in its function. The motor cycle can be summarized as follows[22,23] **(Figure 4)**.

① **Attachment to Microtubule:** The initial step of the motor cycle involves the attachment of dynein to the microtubule. In this state, the AAA1 site of dynein is typically empty, allowing it to bind and establish its connection with the microtubule.

② **ATP Binding and Linker Bending:** Upon ATP binding to the AAA1 site, a conformational change occurs within dynein. This conformational change induces detachment of dynein from the microtubule and triggers a bending motion, called “pre-power stroke”, in the linker region. This bending motion is a critical step in preparing dynein for the subsequent stages of the motor cycle.

③ **ATP Hydrolysis and Phosphate Release:** Following the linker bending, ATP bound to the AAA1 site is hydrolyzed, resulting in the release of phosphate[22]. This phosphate release event is a key energy-releasing step that provides the driving force for dynein's motor activity.

④ **Rebinding to Microtubule:** After ATP hydrolysis, dynein rebinds to the microtubule, preparing for the next step in the motor cycle. This rebinding ensures that dynein remains associated with the microtubule and maintains its position for the subsequent actions.

⑤ **Linker Straightening (Power Stroke):** The reattachment of dynein to the microtubule

leads to straightening of the previously bent linker region, called “post-power stroke”. This straightening motion generates the power stroke, propelling dynein forward along the microtubule. The power stroke is responsible for the movement of dynein and its associated cargo in a directed manner.

This motor cycle model has been extensively supported by studies focused on cytoplasmic dynein, providing valuable insights into its mode of action. While the motor cycle of axonemal dynein is believed to be largely similar to that of cytoplasmic dynein, further investigations are warranted to explore any potential variations or adaptations specific to axonemal dynein.

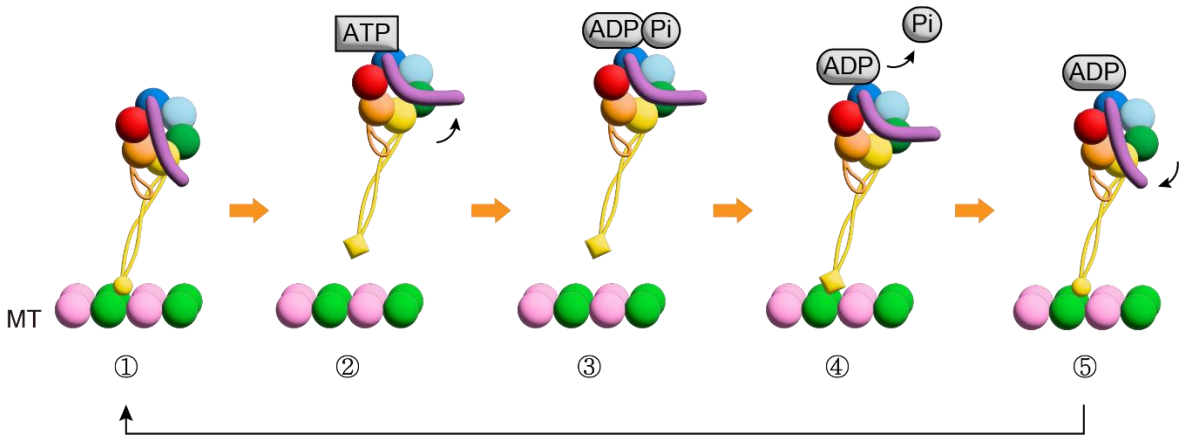

Figure 4. Model for dynein motor mechanism

This schematic diagram (modified from Schmidt & Carter, 2016) illustrates the proposed model for the dynein motor cycle. Detailed mechanisms for each step are interpreted in the context. The MTBD region is represented by two different conformations: a circle (indicating high-affinity to the microtubule) and a diamond (indicating low-affinity to the microtubule).

Dynein conformational change

The movement of dynein is accompanied by attachment and detachment of MTBD to the microtubule, which is synchronized with ATP-hydrolysis in the AAA^+ ring. To accomplish this activity, intramolecular communication between the AAA^+ ring and MTBD is required, which are separated by about 15 nm[24].

This communication occurs via the long coiled coil region that acts as a mediator due to its unique architecture and physical distance. The mechanism of intramolecular communication is explained by the original or modified helix sliding model, whereby the half-heptad shift between two coiled coil helices in α or +β registry leads to specific MTBD conformations of high or low affinity to the microtubule[25–27] **(Figure 5)**.

Results from the microtubule co-sedimentation assays of engineered dynein suggest both axonemal and cytoplasmic dynein possess the two coiled coil conformations of high binding affinity α and low affinity +β registry to the microtubule[27,28].

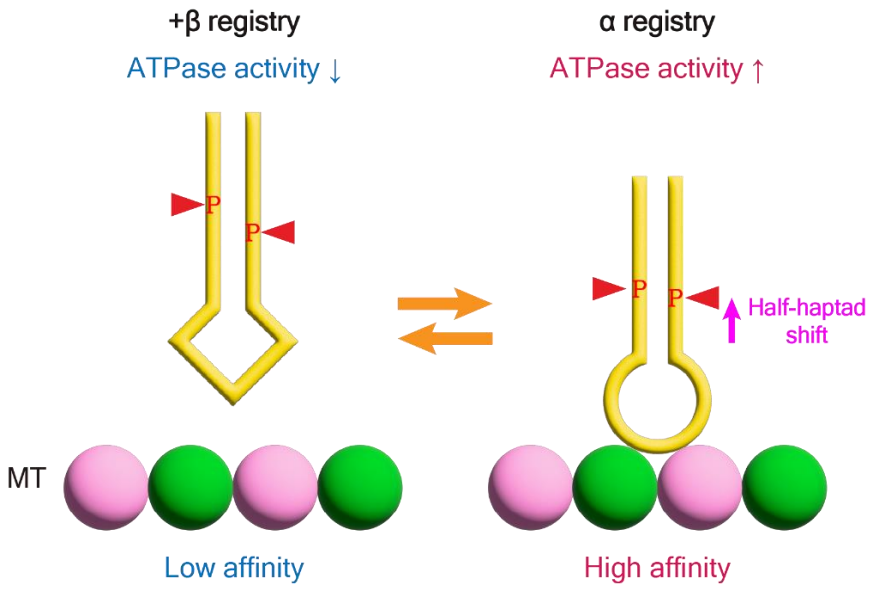

Figure 5. Dynein conformational change model

This schematic diagram illustrates the different conformations of dynein in the high-affinity alpha and low-affinity beta registry. The dynein stalk and MTBD region are depicted as yellow sticks. Conserved proline residues are highlighted in red letters and indicated with arrows.

1.2 Research plan

The research objective of this PhD project is to investigate the functional mechanisms of dynein, a microtubule-based motor protein, by conducting structural studies on its two major types: axonemal and cytoplasmic dynein. Both types of dynein play crucial roles in ciliary movement and intracellular transport, and their dysfunction has been linked to various diseases. However, the available structural information in the Protein Data Bank has a significant bias towards cytoplasmic dynein, necessitating a comprehensive exploration of axonemal dynein.

The primary chapter of this thesis will begin with a structural study of the human inner-arm dynein-d stalk and MTBD construct using X-ray crystallography. This investigation aims to enhance our understanding of inner-arm dynein, as the current knowledge is limited to a few MTBD-only structures, while a well-defined architecture has been recently proposed for the outer-arm dynein complex through Cryo-Electron microscopy (EM) studies.

While there are numerous Nuclear magnetic resonance (NMR), X-ray, and Cryo-EM structures available for cytoplasmic dynein, there is less atomic-level studies on the interaction between the cytoplasmic dynein MTBD and microtubules due to inherent limitations. To address this limitation, my research focus will expand in the following chapter to include complex structure studies of a human SRS-fused dynein stalk and MTBD construct with porcine tubulin. This study aims to elucidate the underlying mechanisms of interaction between dynein and microtubules at the atomic level.

By conducting these structural studies on axonemal and cytoplasmic dynein, this project seeks to uncover novel insights into the functional mechanisms of dynein. Our findings will contribute to a deeper understanding of the roles played by these motor proteins in cellular processes, potentially leading to advancements in the diagnosis and treatment of dynein-associated diseases.

Chapter 2

Human inner-arm dynein heavy chain d stalk and MTBD

2.1 Introduction

This chapter focuses on our investigation into the structure and function of axonemal dynein, a motor protein that plays a crucial role in cellular movement and is linked to hereditary disorders such as PCD[16] and sperm dysmotility[29]. I began by examining the relatively small and mobile stalk regions of human axonemal inner-arm dynein-d (DNAH1s), which have not been structurally characterized at the atomic resolution, despite recent cryo-EM structures providing insight into axonemal dynein complexes.

I have solved the X-ray structure of human inner-arm dynein-d stalk (DNAH1s) at 2.7 Å resolution using the single-wavelength anomalous dispersion (SAD) method and compared it with the available structures in the Protein Data Bank. My analysis revealed that the overall structure of the DNAH1s MTBD showed a high similarity to those of OADγ[30], dynein-c[28], and DNAH7[31], but the distinctively extending flap region implied an isoform-specific functional role depending on each intracellular sublocation.

Since only my DNAH1s structure includes the long coiled coil region with well-resolved side chain information, I am able to analyze its coiled coil packing and registry. Comparison with that of cytoplasmic dynein structures from *Dictyostelium discoideum*[32] and *Mus musculus*[25] highlights the type-specific structural difference in the stalk region between cytoplasmic and axonemal dynein.

Finally, I discussed the distinct structural features of axonemal dynein MTBD caused by different localization compared with cytoplasmic dynein. My findings provide new insights into the molecular mechanism of axonemal dynein and could have potential implications for the development of therapeutics for PCD and other related disorders.

2.2 Materials and Methods

Molecular Cloning and Expression

The DNA sequence encoding a region of the *Homo sapiens* inner-arm dynein heavy chain d stalk and MTBD construct (Glu2844 to Gly3120) was amplified from Human DNAH1 cDNA, purchased from Kazusa DNA Research Institute. The amplified gene was then inserted into the pET17b vector, which contains an ampicillin-resistant gene and a TEV cleavage site, followed by an N-terminal hexa-Histidine tag. The resulting DNAH1s recombinant plasmids were transformed into *E. coli* BL21(DE3) competent cells for protein expression.

A fresh cell colony from a successful transformation in BL21(DE3) expression cells was inoculated into a 200 mL starter culture of sterilized Luria-Bertani (LB) broth containing 100 μg/mL ampicillin. The starter cultures were grown for 16 hours in a shaking incubator at 180 rotations per minute (rpm) at 310 K. To overexpress the protein, 15 mL of the starter culture was used to inoculate a 1.5 L fresh LB broth with 100 μg/mL ampicillin. The total culture volume of 6 L was then incubated at 310 K, shaking at 120 rpm. Cell growth was monitored by measuring the optical density at 600 nm (OD_{600}) using a spectrophotometer. When the OD_{600} value reached a range of 0.6 to 0.8, cells were induced by adding 0.5 mM isopropyl β-D-1-thiogalactopyranoside (IPTG) and incubated for 16 hours at 293 K. The cells were harvested by centrifugation and stored at 193 K before the cell lysis step for protein purification.

To produce samples for SAD phasing, B834 (DE3) pLysS cells were used instead of BL21(DE3) and cultured in LeMaster medium containing 5 μg/mL Vitamin B1 and 25 μg/mL L-selenomethionine (SeMet).

Purification

For the first step, the frozen cell pellets were thawed and resuspended in 100 mL of His A buffer [50 mM Tris-HCl pH 8.0, 100 mM NaCl] supplemented with two tablets of cOmplete™, EDTA-free Protease Inhibitor Cocktail (Roche). The cells were lysed by 4-5 rounds of sonication on ice, and the lysate was clarified by ultracentrifugation at 200,000 × g for 30 minutes at 277 K. The supernatant was loaded onto a 5 mL HisTrap HP column (Cytiva) that had been pre-equilibrated with 5 column volumes (CV) of His A buffer, at a flow rate of 5 mL/min using a peristaltic pump at 277 K. To increase the efficiency of capturing the target protein, the flow-through was recirculated for 30 minutes.

After connecting the sample-loaded column to the ÄKTA FPLC (Cytiva), the column was washed with 20 CV of His A buffer and 2% of His B buffer [50 mM Tris-HCl pH 8.0, 100 mM NaCl, 500 mM imidazole] to remove nonspecific binding proteins. The target proteins were eluted by a gradient from 10 to 500 mM imidazole for 20 CV, and the eluted samples were collected in 1 mL fractions. The purity of the proteins in the fractions was analyzed by Sodium dodecyl sulfate-polyacrylamide gel electrophoresis (SDS-PAGE), and the fractions containing the protein of interest were pooled for the TEV cleavage step. Hexa-histidine tags of DNAH1s were eliminated by adding 1/70 (w/w) TEV protease, and the sample including buffer was exchanged to the SEC buffer [10 mM Tris-HCl pH 8.0, 100 mM NaCl] by dialysis at 277 K overnight.

Successfully cleaved proteins were collected by the flow-through of an additional Ni-immobilized metal affinity chromatography (IMAC) step and loaded onto a HiLoad 16/600 Superdex 200 pg column (Cytiva) pre-equilibrated with 2 CV of SEC buffer. Fractions containing DNAH1s were pooled and concentrated up to 15 mg/mL using an Amicon Ultra-4 Centrifugal Filter Unit [10 kDa Molecular weight cut-off (MWCO); Millipore] for crystallization. The sample was stored at -80 °C until use.

The SeMet-substituted proteins were purified using the same protocol as for wild-type protein purification described above.

Crystallization and X-ray data collection

The initial screening for crystallization of DNAH1s utilized the sitting-drop vapor diffusion method. Crystallization droplets were formed by mixing 200 nL of the native target protein at a concentration of 15 mg/mL, dissolved in SEC buffer, with an equal volume of commercially available reservoir solution from Hampton Research using a mosquito LCP (SPT Labtech).

Subsequently, initial crystals of DNAH1s were obtained and further optimized by adjusting the concentration of salt and precipitation to achieve suitable quality for structural determination. Optimization droplets were produced by manually mixing 1 μL of the sample with an equal volume of reservoir solution using the hanging-drop vapor diffusion method. The SeMet derivative samples were crystallized under the same optimized condition as the native crystal.

Both native and SeMet derivative crystals were briefly soaked in a cryoprotectant solution and then flash-cooled in liquid nitrogen. X-ray diffraction data were collected at the Super Photon Ring-8 GeV (SPring-8) beamline BL44XU.

Structure determination

The collected diffraction images were processed using the XDS software[33]. The positions of Se atoms were located using SHELXC/D, and automatic phasing was performed using the Autosol program from the PHENIX package[34,35]. The initial model was built using the AutoBuild program in PHENIX, and further manual building was performed using the Coot software[36]. The structure refinement was carried out using the phenix.refine program[37,38] at a resolution of 2.7 Å, and the final refined structure was deposited in the Protein Data Bank with accession number 8I3J. The crystallographic data and refinement statistics are shown in **Table 1**.

Coiled coil Packing and Domain Angles analysis

To analyze the knobs-into-holes packing and heptad repeat of the DNAHs stalk region, SOKET2 software[39,40] was used with a packing-cutoff of 7.0 Å. The antiparallel coiled coil region was detected between Leu2853 to Ala2909 and Lys3056 to Cys3112, and the heptad repeat was represented by the continuous letters of abcdefg. The continuity of the detected coiled coil region was further confirmed using the TWISTER program[41]. To analyze the domain angles, the stalk regions from each N and C-terminus to conserved proline residues were selected as the fixed domain, while the rest of the MTBD regions were selected as the moving domain using the Domain Select option in DynDom[42].

2.3 Results

Purification

To initiate the purification process of DNAH1s, the cell lysate was loaded onto a 5 mL HisTrap HP column (Cytiva) following cell lysis. Non-specifically bound proteins were subsequently removed by washing the resin with 10 mM imidazole, and the target proteins were then eluted with 500 mM imidazole. Elution fractions were collected within the range of 62 to 110 mL in 1 mL increments and assessed for yield and purity using SDS-PAGE analysis **(Figure 6)**. Fractions containing the desired proteins were retained for further purification steps.

To ensure that the maximum injection volume for gel filtration was not exceeded, the DNAH1s proteins, with the affinity tag removed by TEV cleavage, were concentrated to a volume of 2 mL and applied onto a pre-equilibrated HiLoad 16/600 Superdex 200 pg column (Cytiva) with SEC buffer. Following elution, peak fractions ranging from 41 to 82 mL were collected and analyzed through SDS-PAGE **(Figure 7)**. Although some contaminant proteins persisted after the two-step purification, the purity of the target protein displayed a notable improvement compared to the previous stage. The purest elution fractions of DNAH1s were subsequently concentrated to a concentration of up to 16 mg/mL, preparing them for the crystallization step.

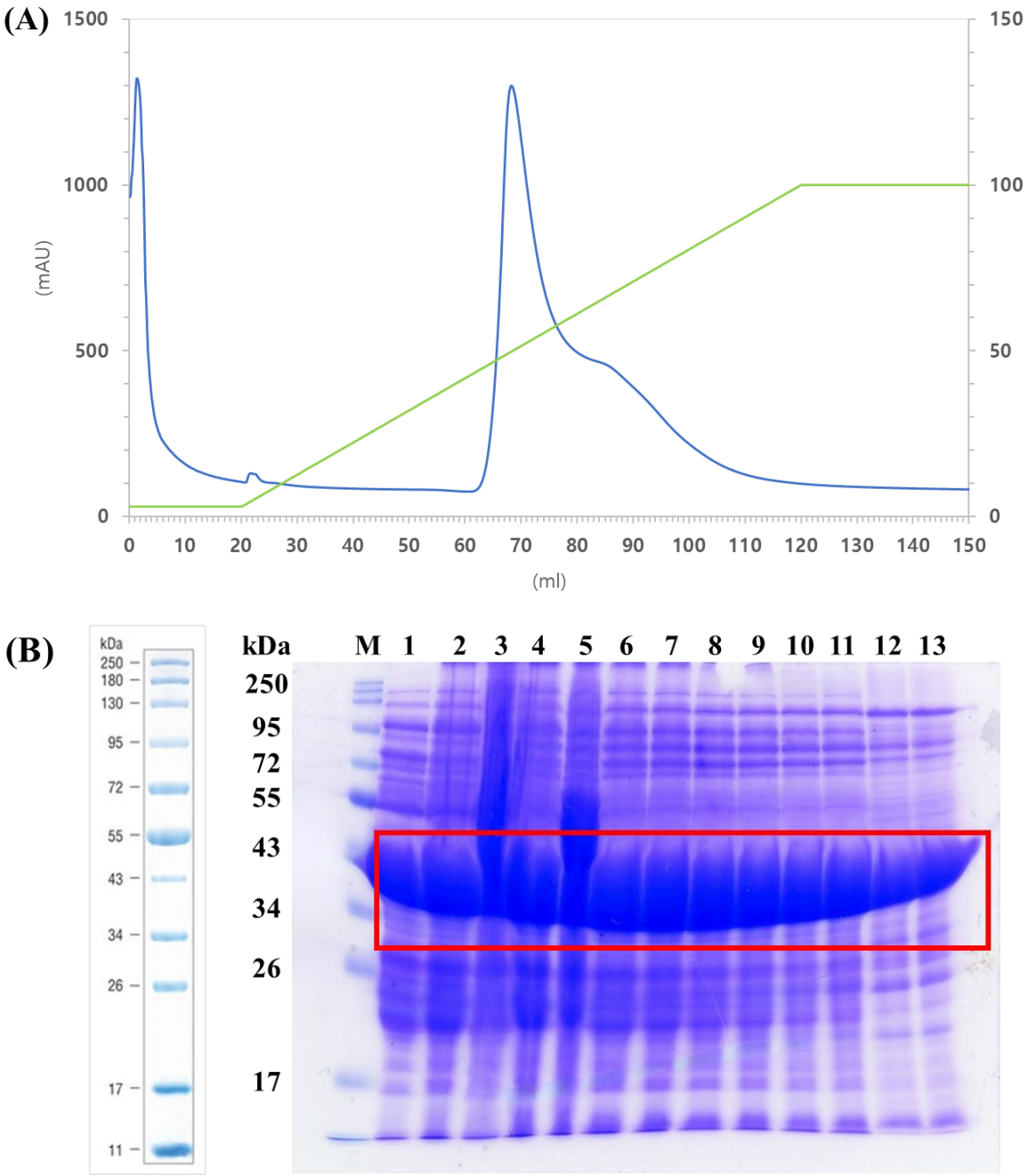

Figure 6. Affinity chromatography result of DNAH1s

(A) Elution profile of affinity chromatography with UV trace at 280 nm (blue). DNAH1s eluted with a peak at fractions between 62 and 110 mL.

(B) SDS-PAGE result of IMAC. The left-side image illustrates the entire size of the protein molecular weight marker [Blue Prestained Protein Standard, Broad Range (11-250 kDa; NEB)]. Information for the loaded fractions is as follows:

M: Molecular weight marker, Lane 1-13: 1 mL elution fractions from 64-77 mL. Target proteins are highlighted in the red box.

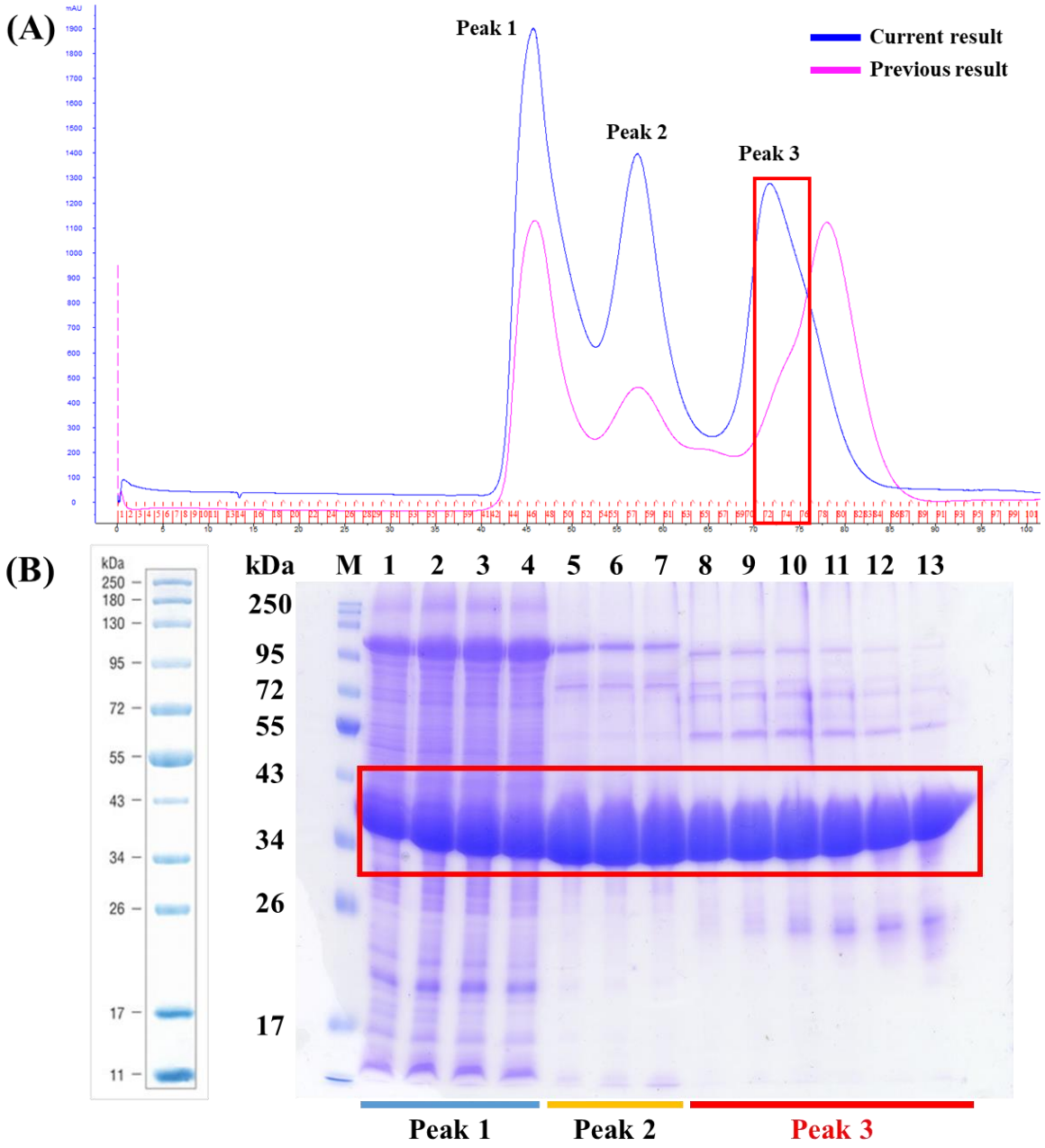

Figure 7. Size-exclusion chromatography result of DNAH1s

(A) Elution profile of gel filtration with UV trace at 280 nm (blue). DNAH1s eluted with three peaks at fractions between 41 and 82 mL.

(B) SDS-PAGE result of SEC. The left-side image illustrates the entire size of the protein molecular weight marker. Information for the loaded fractions is as follows: M: Molecular weight marker, Lane 1-4: 1 mL elution fractions from 44-48 mL, Lane 5-7: 1 mL elution fractions from 56-60ml, Lane 8-13: 1 mL elution fractions from 70-76 mL. Target proteins are highlighted in the red box.

Crystallization and X-ray data collection

DNAH1s crystals were produced at 277 K and optimized to a sharp-edged prism-like shape in a condition of 0.25 M potassium sodium tartrate tetrahydrate and 22% PEG 3350 using the hanging-drop vapor diffusion method **(Figure 8A)**. Subsequently, X-ray diffraction data were collected from the obtained crystals **(Figure 8B)**. The obtained crystals belong to a hexagonal space group of $P6_122$, with unit cell parameters $a = b = 147.47$ Å and $c = 85.08$ Å. The Matthews coefficient (V_M) of the crystal was estimated to be 4.3 $Å^3$/Da, and its solvent content was 71.38%.

Initial molecular replacement (MR) using the predicted model by ColabFold[43] as a search model failed to provide feasible solutions for crystallographic phase information. Instead, SAD phasing was employed, using proteins in which methionine was substituted by SeMet. The initial map obtained after density modification, calculated at 2.9 Å resolution, was clear enough to build the backbone of the molecule, and the final model structure was refined with 2.7 Å data. Detailed crystallographic data can be found in **Table 1.**

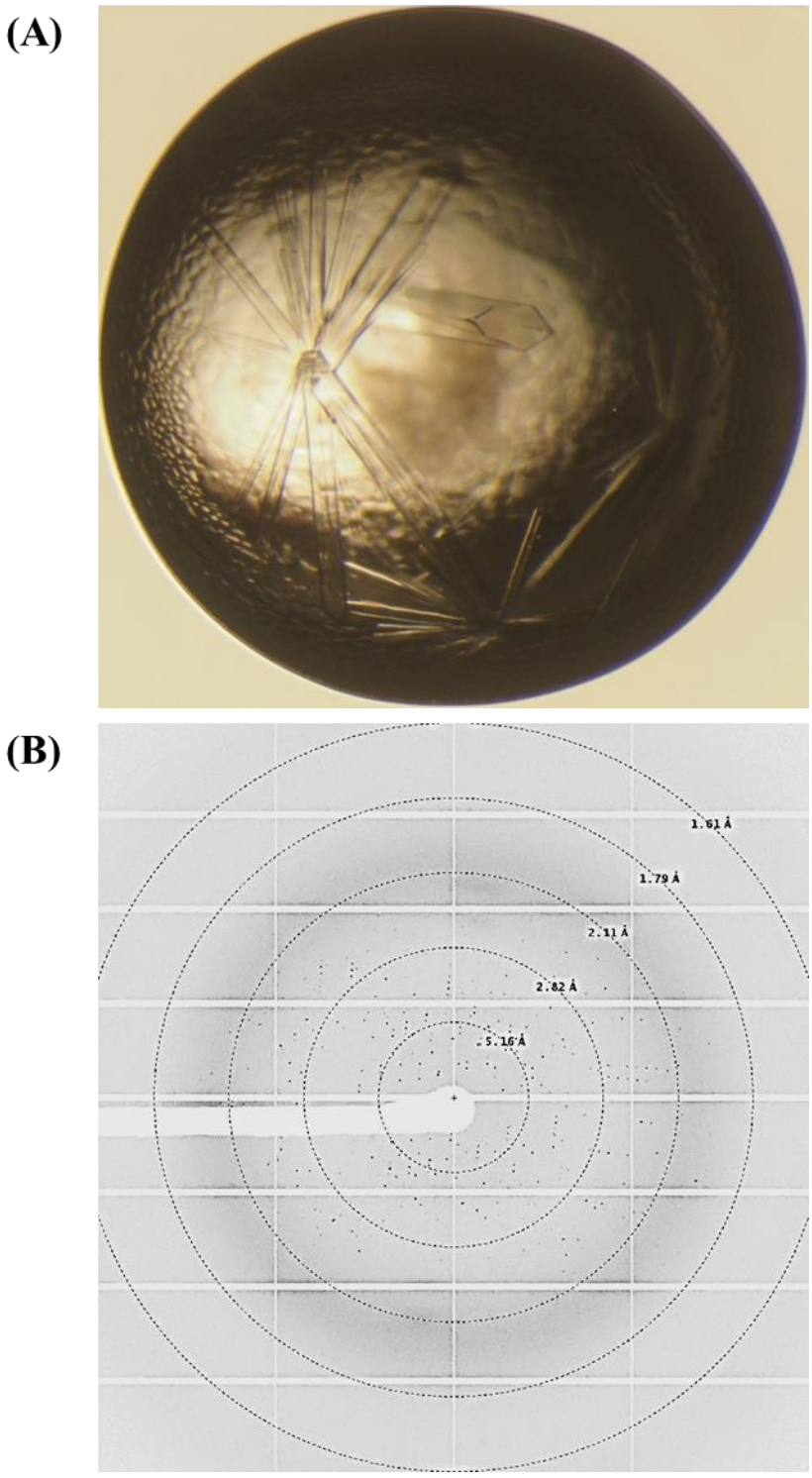

Figure 8. DNAH1s crystals and X-ray diffraction data

(A) Sharp-ended prism shape crystals in the condition of 0.25 M potassium sodium tartrate tetrahydrate and 22% PEG 3350.

(B) X-ray diffraction image from a DNAH1s crystal.

Table 1. Data collection and refinement statistics.

Data Collection	*DNAH1s*
Beamline	SPring-8 BL44XU
Wavelength (Å)	0.97938
Resolution range(Å)	38.07 - 2.69 (2.786 - 2.69)
Space group	$P6_122$
Unit cell (*a*, *b*, *c*/Å, α, β, γ/°)	147.47, 147.47, 85.08, 90, 90, 120
Total reflections	602,551 (55,974)
Unique reflections	15,600 (1,509)
Redundancy	38.6 (37.1)
Completeness (%)	98.65 (97.05)
Mean I/sigma(I)	24.83 (2.49)
Wilson B-factor (Å^2)	83.24
R-meas	0.1248 (2.489)
CC1/2	1 (0.968)
Refinement	
Reflections used in refinement	15,432
Reflections used for R-free	782
R-work/R-free	0.2582/0.2679
Number of non-hydrogen atoms	2,172
macromolecules	2,172
ligands	0
solvent	0
Protein residues	277
RMS (bonds, Å)	0.010
RMS (angles, °)	1.42
Ramachandran	
favoured (%)	95.64
allowed (%)	3.64
outliers (%)	0.73
Average B-factor	121.64

Statistics for the highest-resolution shell are shown in parentheses.

Overall structure of DNAH1s

The DNAH1s construct from *Homo sapiens* consists of a total of 282 amino acid residues, ranging from Glu2844 to Gly3120, including the stalk [Coiled coil (CC); CC1:CC2=77:69) and the MTBD region. The final refined model contains one molecule of DNAH1s in the crystallographic asymmetric unit, consisting of two long antiparallel coiled coil helices of the stalk connected to the globular MTBD, which includes 8 short helices and one extended β-hairpin flap **(Figure 9)**. This architecture, excluding the flap, is highly similar to that of cytoplasmic dynein structure, despite the difficulty in finding a sequences similarity between cytoplasmic and axonemal dyneins (sequence identity is lower than 30%; **Figure 10**).

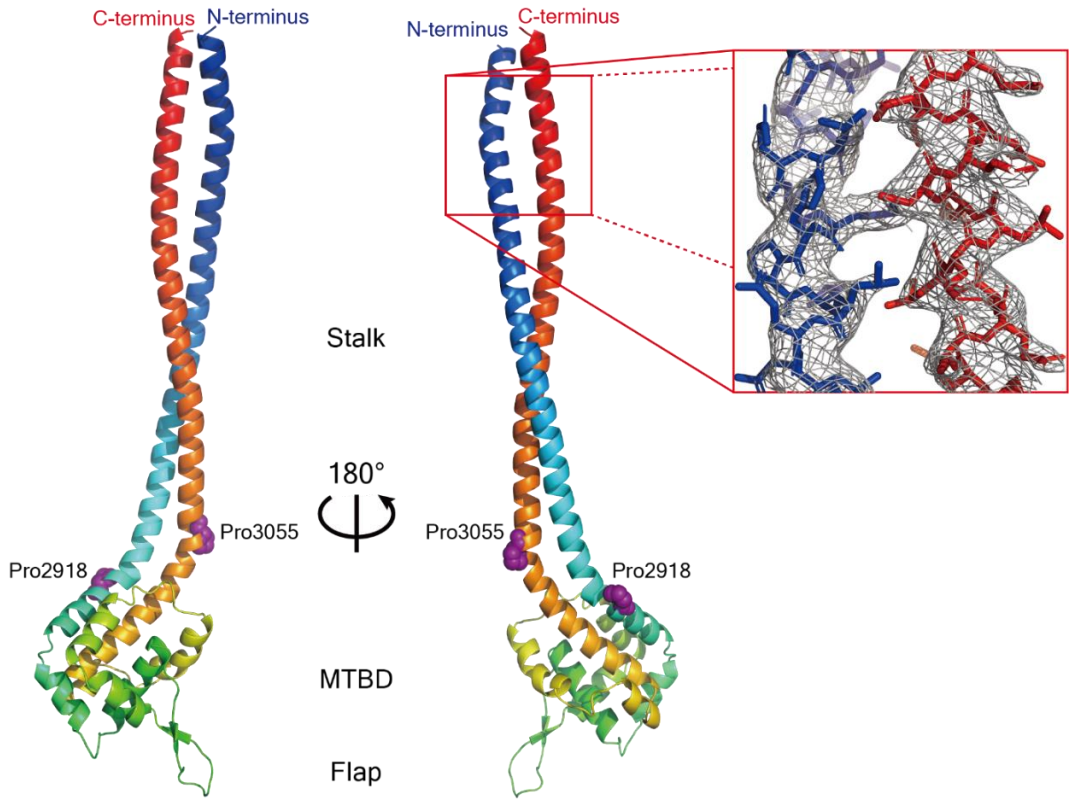

Figure 9. Overall structure of DNAH1s

Left: Ribbon structure of inner-arm dynein-d (DNAH1) stalk and MTBD. Conserved Proline residues are drawn as CPK model (purple). Right: Rotated view of DNAH1s structure. Slight kinked region in N-terminus is highlighted in red box as a stick model with electron density map (grey).

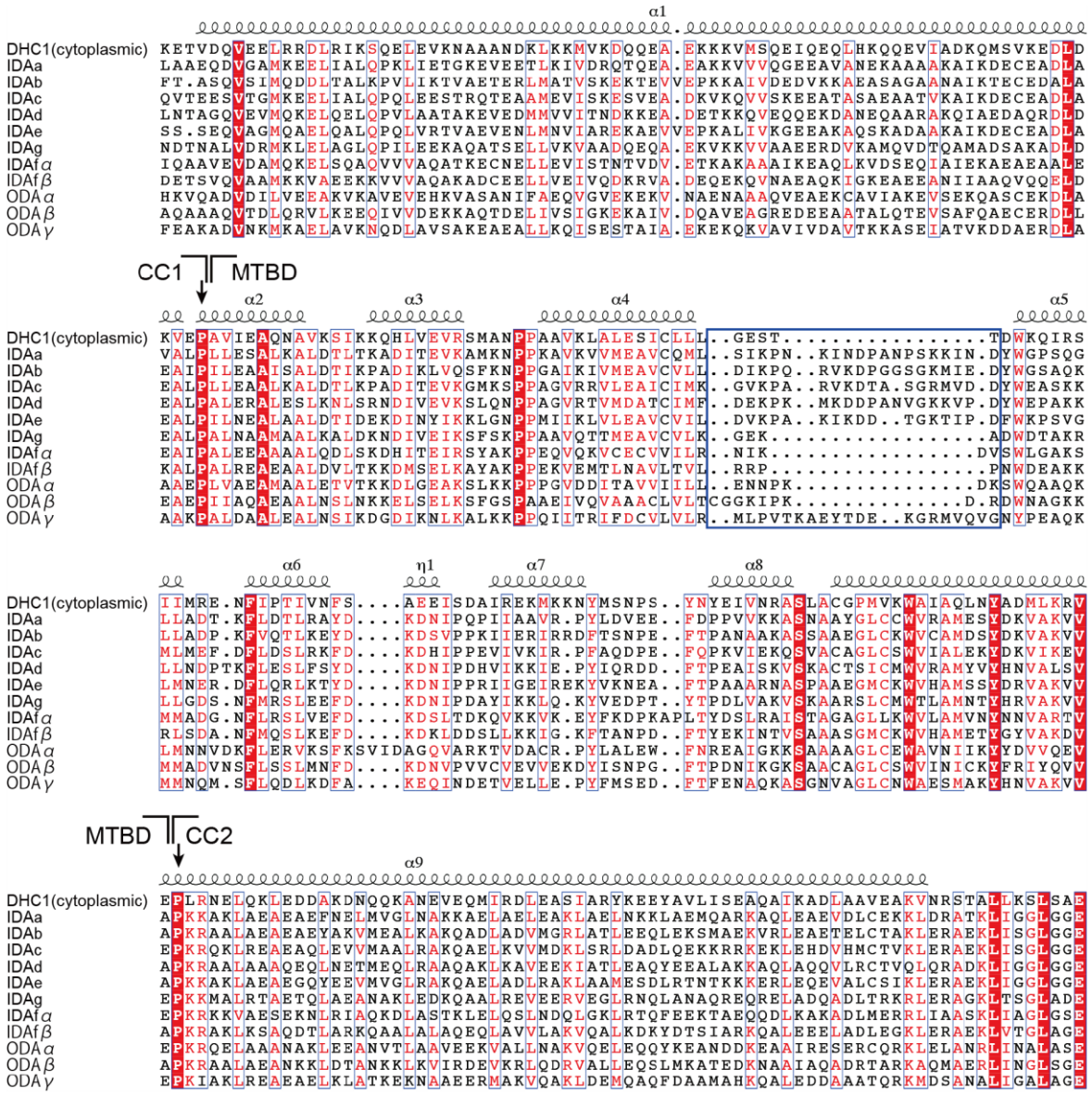

Figure 10. Sequence alignment of axonemal dynein MTBDs from *Chlamydomonas reinhardtii*

Amino acid sequences of DHC1 (UniProtKB: Q14204), IADa (UniProtKB: A8I5C3), IADb (UniProtKB: A8I3X6), IADc (UniProtKB: Q4AC22), IADd (UniProtKB: A8J063), IADe (UniProtKB: A8ISA6), IADfα (UniProtKB: Q9SMH3), IADfβ (UniProtKB: Q9MBF8), IADg (UniProtKB: A8IV22), OADα (UniProtKB: A8J336), and OADβ (UniProtKB: A8J1M5), OADγ (UniProtKB: A8JFP1) were aligned by CLUSTALW. Flap motif regions are highlighted in blue box.

Compared to publicly available axonemal dynein stalk structures of DNAH7 [Protein Data Bank (PDB) ID: 6RZA], dynein-c (PDB ID: 2RR7), and OADγ (PDB ID: 6L4P), the DNAH1s structure only includes the long coiled coil region, which is important for registry analysis to understand the helix sliding model in terms of dynein affinity change to the microtubule. The detailed coiled coil registry of DNAH1s will be investigated in the following section.

Interestingly, the N-terminal tip of the stalk coiled coil of DNAH1s is slightly kinked, while that of OAD shows a different direction and angle of kink **(Figure 9, 11a)**. This feature may be a characteristic of axonemal dynein, as the amino acid sequence in the kinked region is relatively less conserved compared to other regions, as determined by the ConSurf server[44] (**Figure 11b**). The unique extension of flap motif also displays low amino acid sequence conservation.

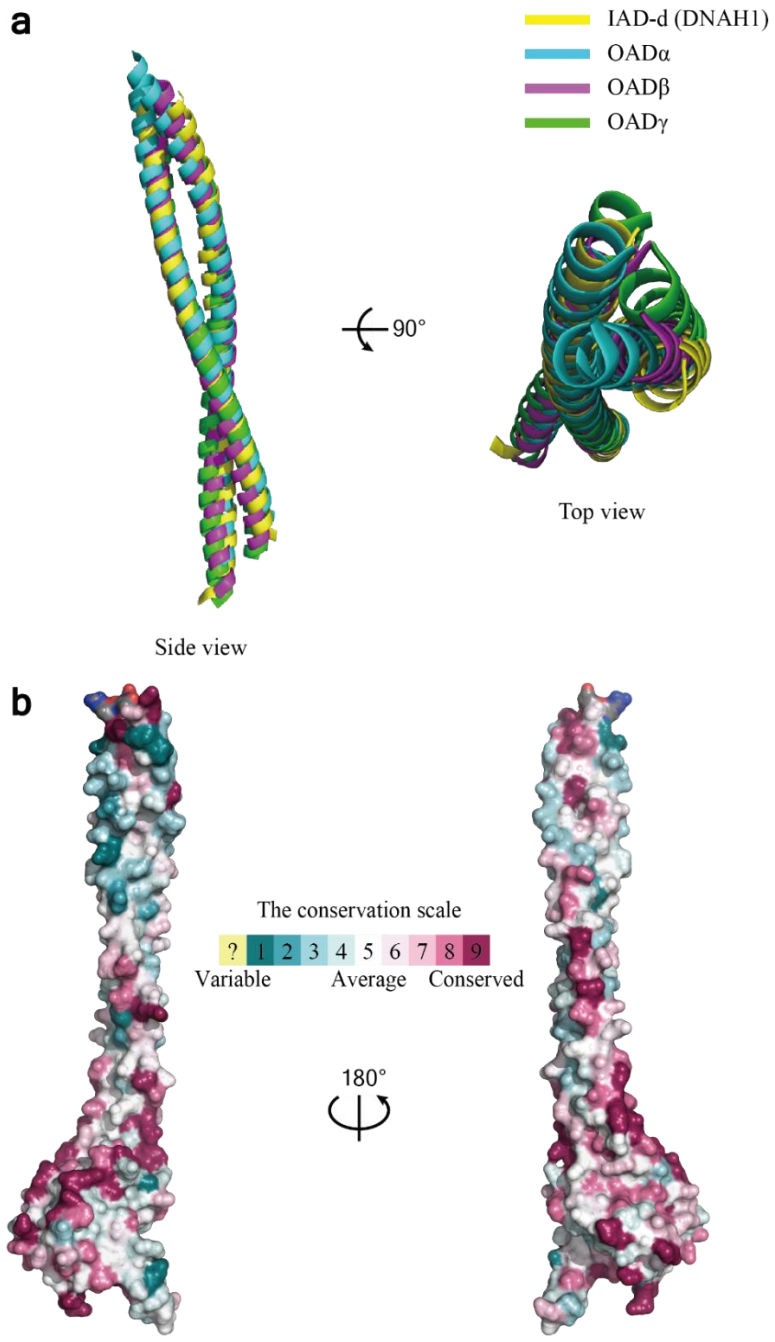

Figure 11. Structural comparison and amino acid conservation analysis of DNAH1s

(a) Structural comparison of the stalk region between DNAH1s and OAD isoforms (PDB ID: 7KEK) from *Tetrahymena thermophila*. The CC1 regions of all presented axonemal dyneins exhibit unique kink, which should be further confirmed by a high-resolution structure of OAD, as their current resolution is 8.0 Å.

(b) ConSurf analysis of amino acid conservation in DNAH1s. The ribbon model of DNAH1s structure is colored from deep teal to deep purple, indicating variable to conserved regions, based on the ConSurf analysis of evolutionary conservation of amino acids.

Coiled coil packing and registry analysis

Previous research has shown that the stalk coiled coil of axonemal dynein has two structural conformations, α and +β registry, which exhibit high and low affinity to microtubules, respectively, similar to cytoplasmic dynein[27,28]. The registry conversion occurs along the packing of two coiled coil helices in the stalk region, which is explained by the helix sliding model[25–27] **(Figure 12a)**, including modified models such as helix melting, winding, or zippering. To determine the binding conformation of DNAH1s to microtubules, knobs-into-holes (KIH) packing and heptad repeats, the hallmark of coiled coil assemblies, were analyzed using SOCKET2 software[39,40] **(Figure 12b)**. The analysis identified an antiparallel coiled coil packing in the range of Leu2853 to Ala2909 in CC1 and Lys3056 to Cys3112 in CC2 of the stalk region of DNAH1, with a total of 27 amino acid residues (12 in CC1 and 15 in CC2; highlighted in red letter in **Figure 12b**) included as knobs in this interaction.

For comparison, the stalk coiled coil structures of cytoplasmic dynein from *Dictyostelium discoideum* (ΔMTBD) and *Mus musculus* (Stalk277), whose registry is α and +β, respectively, were analyzed using SOCKET2 in the same way **(Figure 12c-d)**. Based on the positions of conserved Pro residues (Pro2918 and Pro3055), α-helical registry of DNAH1s was assigned as +β, but the number of residues involved in the KIH packings was quite different from that in the Stalk277 structure with +β registry. The KIH packings of DNAH1s (27 residues) were spread over the entire coiled coil region, while those of Stalk277 (23 residues) were absent in the N- and C-terminal parts, and those of ΔMTBD (26 residues), whose helical registry was α, appeared similar to that of DNAH1s.

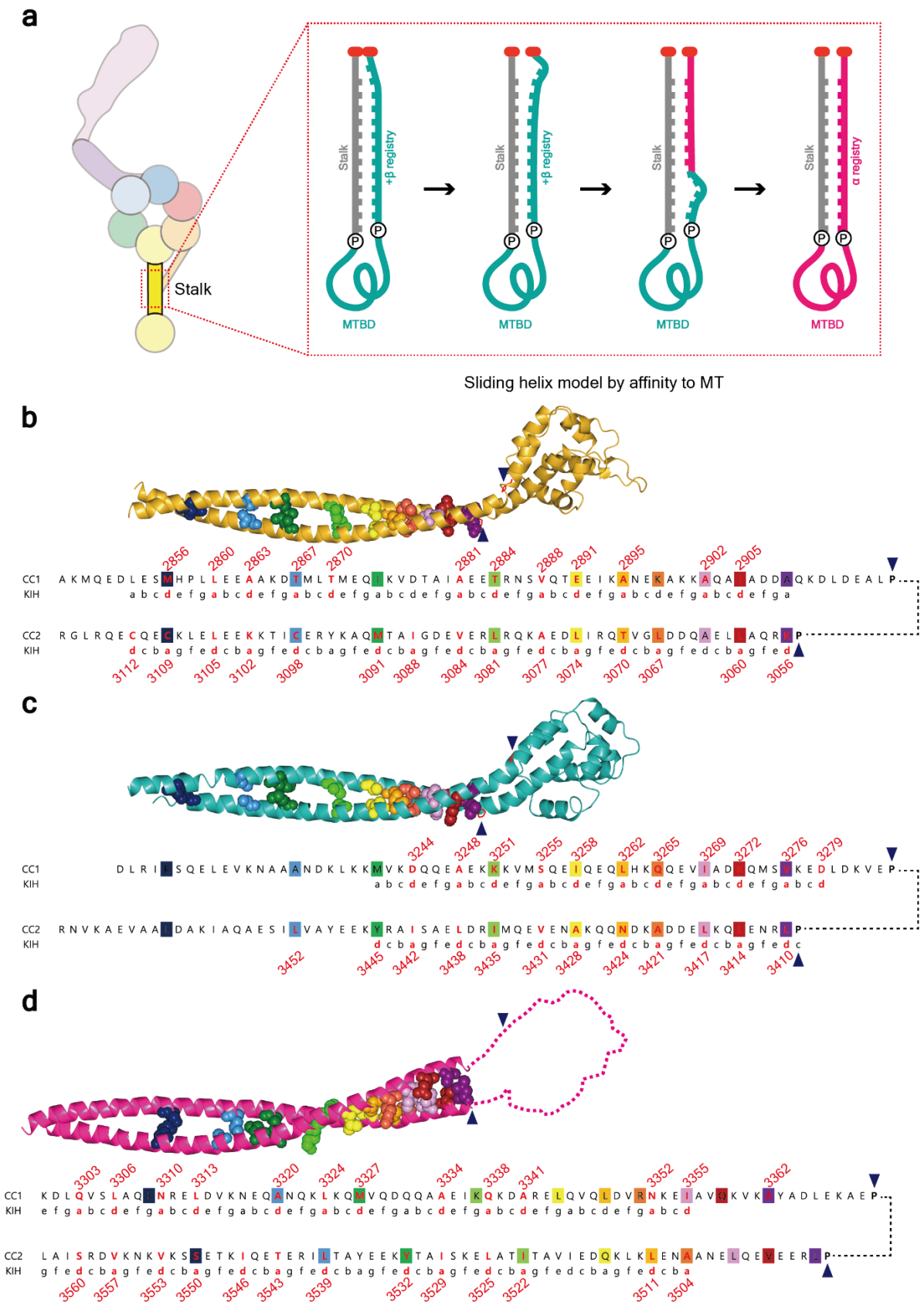

Figure 12. Registry conversion model and KIH packing analysis

(a) Schematic diagram of registry conversion from +β to α registry, showing four stages: 1) fully zipped-up +β registry (teal), 2) partial zip-off +β registry (teal), 3) intermediate stage with partial zip-off and helix sliding (magenta and teal), and 4) high affinity α registry to microtubule (magenta).
(b-d) Comparison of stalk coiled coil KIH packing and heptad register. Rainbow-colored residues show the identical positions of corresponding residues in the alignment. Residues involved in knobs-into-holes packing are highlighted in red one-letter amino acids codes. Arrowheads (dark blue) indicate the positions of conserved proline residues. (b) DNAH1s (PDB ID: 8I3J), (c) Stalk277 (PDB ID: 5AYH), and (d) ΔMTBD (PDB ID: 3VKG). Coiled coil registry of (b) and (c) are assigned in +β based on the positions of conserved proline residues, whereas the half-heptad shifted (d) is in α registry.

Comparison of MTBD structures

In addition to the structural comparison of the coiled coil stalk region between DNAH1 and available cytoplasmic dynein structures, the rotation and head up angle of the MTBDs with respect to the coiled coil were calculated to analyze the structural differences between the MTBDs of DNAH1s and Stalk277.

Two conserved Proline residues were defined as the ankle, the coiled coil as a leg, and the MTBD as a foot to facilitate better understanding. The structures of the legs were superimposed based on their stalk coiled coil, and the different orientations of the foot domains were analyzed by the DynDom domain movement analysis program[42]. The rotation angle of the moving MTBD domain was found to be 27.2°, while the r.m.s.d. of the fixed coiled coil domain was 2.384 Å **(Figure 13)**. Furthermore, the extent to which the MTBD was headed up against the superposing axis of the long coiled coil was determined using Principal Component Analysis (PCA) **(Figure 14)**, and the raising angle was found to be 10.3 °.

Notably, it was observed that the flap of DNAH1s extended uniquely from the sole of the foot like a spike. Although the structures of DNAH7, dynein-c, or OADγ-LC1 complex all had a flap region, the orientation to be extended varied significantly **(Figure 15)**.

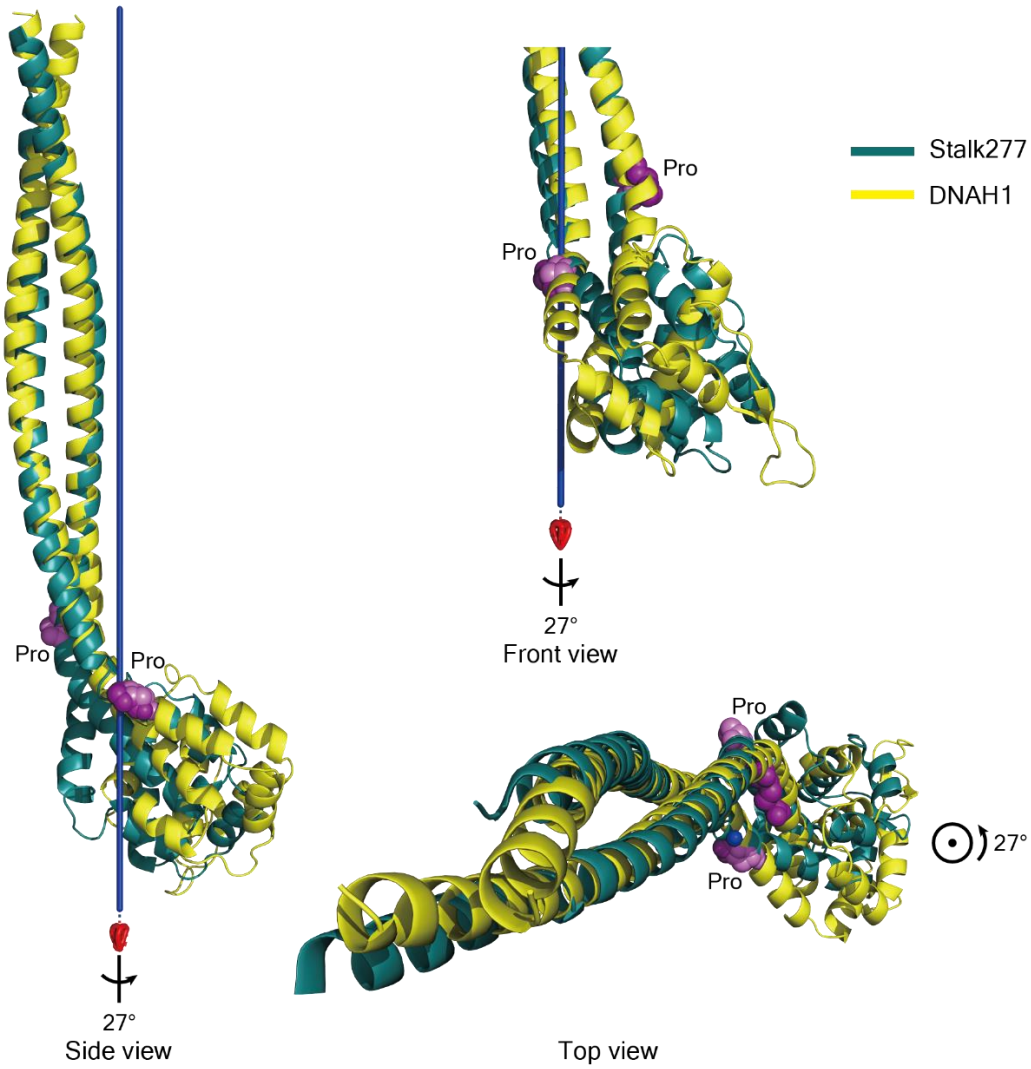

Figure 13. Structural comparison of MTBD regions between DNAH1s and Stalk277

Figure shows the DynDom analysis of the rotation angle between the MTBD regions of DNAH1s (yellow) and Stalk277 (teal) in various views. The conserved proline residues are illustrated as a purple CPK model, and the rotation axis is presented in blue with a red arrowhead.

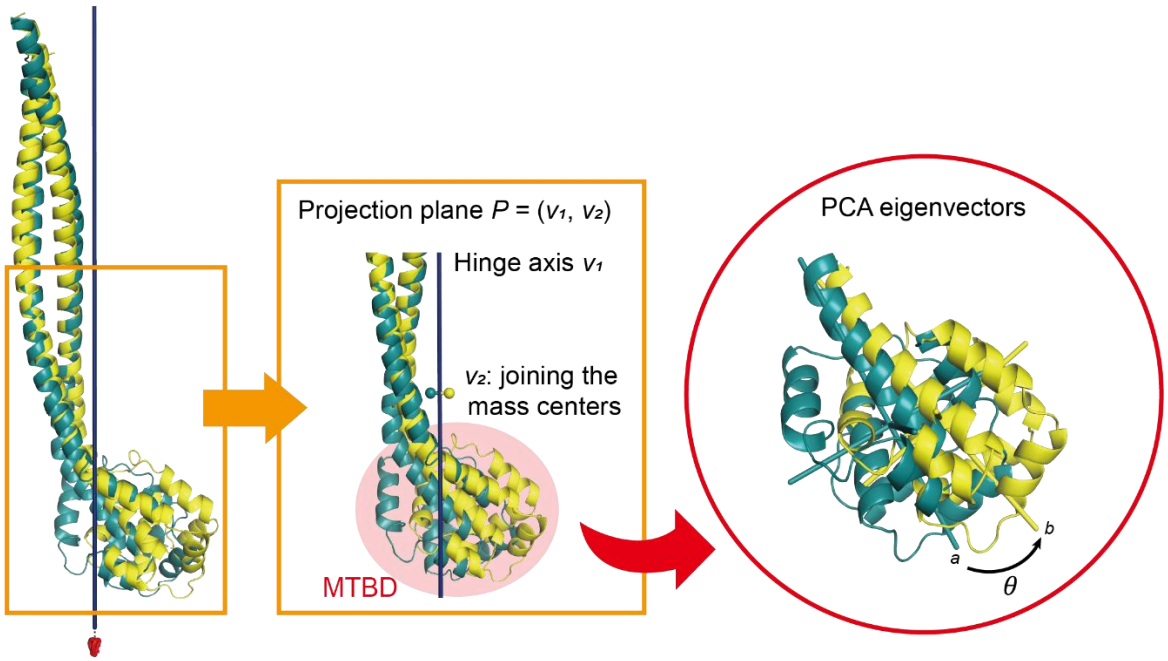

Figure 14. Quantify the rotation angle between axonemal and cytoplasmic dynein MTBDs with Principal Component Analysis (PCA)

1) Two superimposed models of Stalk277 (dark teal) and DNAH1s (yellow) generated by DynDom.

2) A projection plane is defined as $P = (v_1, v_2)$, where vector v_1 is the hinge axis, and v_2 is the vector joining the mass centers of Stalk277 and DNAH1s.

3) The PCA eigenvectors of the MTBDs from Stalk277 and DNAH1s are shown as vectors a and b, respectively. The angle θ represents the rotation angle from vector a to vector b in the plane $P = (v_1, v_2)$.

4) The vector projections of a and b in the plane P can be determined using the following equations:

$$a_{proj} = (v_1, v_2) \bullet a$$
$$b_{proj} = (v_1, v_2) \bullet b$$

5) The rotation angle θ can be calculated using the following equation:

$$a_{proj} \bullet b_{proj} = \|a_{proj}\| \|b_{proj}\| cos\theta$$

which is found to be 10.3 degrees.

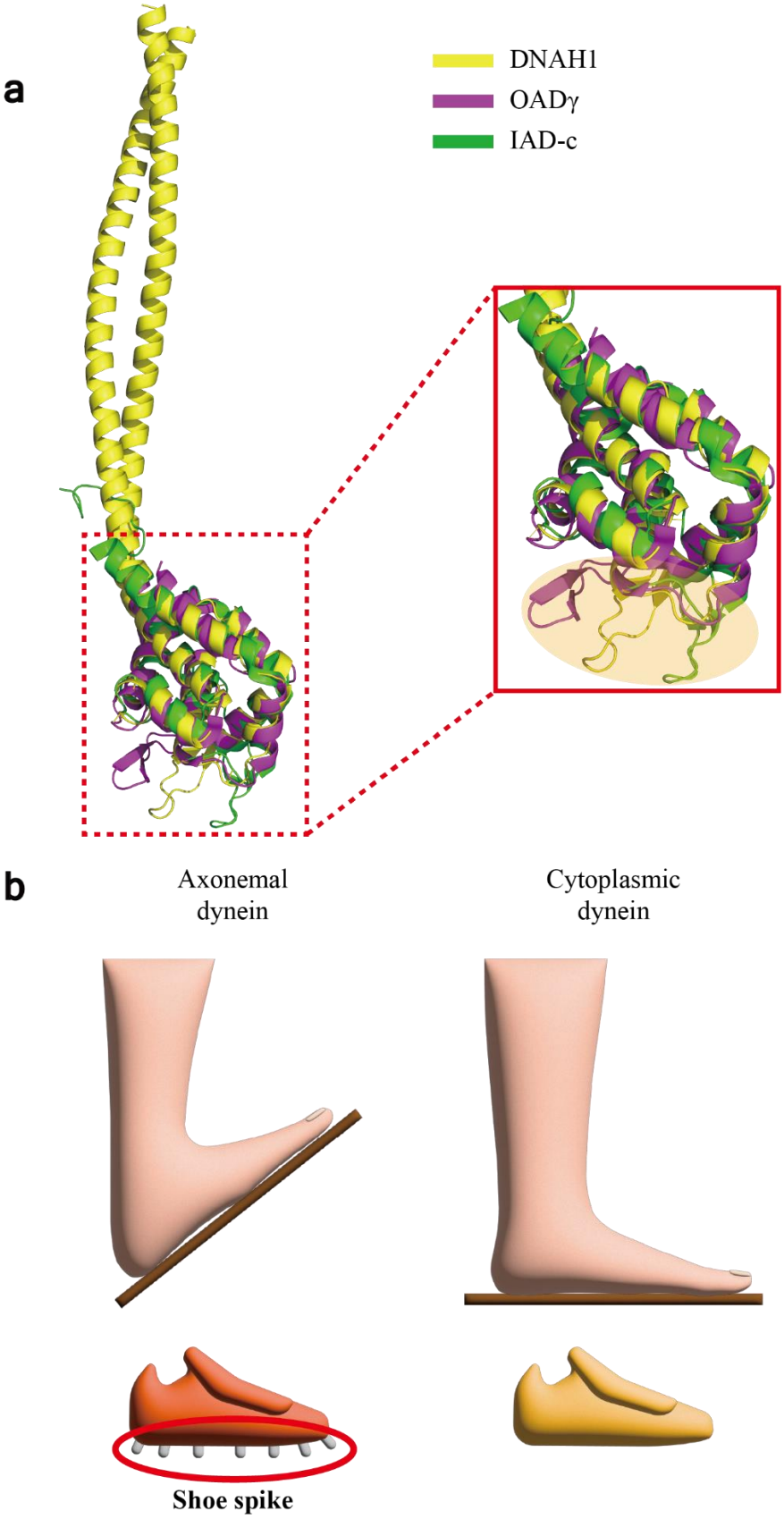

Figure 15. Comparison of flap motif

(a) Figure illustrates the uniquely extended flap regions of DNAH1s highlighted in yellow, IAD-c in green, and OADγ in magenta, respectively. The flap region from the OADγ-LC1 complex has been clipped for better visibility.
(b) Schematic diagram of the proposed "Spike in a Shoe" model. The dynein stalk and MTBD are represented as a human leg and foot, respectively, to aid understanding. The unique positioning of axonemal dynein MTBD on the dynamically moving B-tubule, requires additional assistance like a spike in a shoe to ensure proper attachment.

2.4 Discussion

Advances in structure determination techniques, such as X-ray crystallography, NMR spectroscopy, and cryo-EM, have significantly contributed to our understanding of axonemal dynein motor proteins. However, there is a notable bias in structure determination towards outer-arm dynein compared to inner-arm dynein, despite both types being equally important in biological functions. Cryo-EM studies have provided entire architecture of the outer-arm dynein complex, including its heavy chains (OADα, OADβ, and OADγ) and regulatory proteins (PDB ID: 6ZYW, 7K58, 7K5B, 7KEK). Furthermore, high-resolution X-ray structure of the OADγ-LC1 complex (PDB ID: 6L4P) from my laboratory revealed the atomic resolution structure of MTBD with potential role for the flap motif. However, the structural information on inner-arm dynein is limited to only the MTBD region of DNAH7 (PDB ID: 6RZA) determined by cryo-EM and dynein-c (PDB ID: 2RR7) by NMR, both lacking the stalk coiled coil. Recently, a combination of cryo-EM and AI-based techniques allowed to determine the complete structure of axonemal dynein with doublet microtubules[45]. However, this approach had limitations, as the presented motor domains were predicted by Swiss-model, and no density was observed around the MTBD region. Thus, further research on axonemal inner-arm dynein is necessary to gain a deeper understanding of its mechanism. In this study, I present the first atomic structure of axonemal inner-arm dynein-d stalk, DNAH1s, which includes long coiled coil helices. Our specific focus on the stalk consisting of coiled coil and MTBD regions enables a direct comparison with cytoplasmic dynein structure, benefiting from its high-resolution, including the stalk coiled coil.

Although both axonemal and cytoplasmic dyneins share similar architecture and mechanochemical reactions in an ATP-dependent manner, their cellular localizations differ significantly due to their distinct biological roles. Axonemal dyneins are permanently fixed to

the A-tubule of the outer doublet microtubule and interact temporarily with the adjacent B-tubule to generate movement for cilia and flagella beating[46,47]. In contrast, cytoplasmic dynein complexes with auxiliary proteins to transport cellular cargo directly along microtubules[10,11]. To draw an analogy, cytoplasmic dynein moves like a runner on a regular road, smoothly progressing along a single microtubule, whereas axonemal dynein acts like a mountain climber navigating the doublet microtubule terrain.

Furthermore, the axoneme is densely crowded with various dynein isoforms and doublet microtubules, unlike the cytoplasm. Axonemal dyneins consist of at least 11 isoforms, which is significantly more than the 2 isoforms found in cytoplasmic dynein[20,48]. Due to their physiological function, involving repeating activation and deactivation, the movement of the axoneme becomes dynamic, leading to stressed geometry for each dynein isoform. This has led to the hypothesis that the localization of the microtubule-binding domain (MTBD) from different axonemal dynein isoforms to the B-tubule may vary compared to that of cytoplasmic dynein. To help understanding, I defined the dynein stalk and MTBD as a human leg and foot, respectively. By superposing the DNAH1s structure onto the cytoplasmic Stalk277 based on the leg domain, different orientations of the foot domain were found relative to the leg region. To elucidate these orientation differences, Dyndom and PCA were used to calculate the rotation and elevation angle. The results showed that DNAH1s has a 10.3° foot-up and 27.2° splay foot positioning compared to Stalk277 **(Figure 13, 14)**. This finding suggests that this angular difference can serve as evidence for type-specific movement, supporting the hypothesis.

Additionally, each dynein sub-type is equipped with MTBDs appropriate for their roles in either outer-arm dynein (OAD) or inner-arm dynein (IAD) sub-types, and each MTBD exhibits isoform-specific motor properties. These unique localization features may require additional assistance to ensure proper attachment to the microtubule. I propose a "spike shoes"

model to explain the uniquely extended flap of DNAH1s, which can grip the B-tubule tightly on the doublet microtubule **(Figure 15)**. This model suggests that the various lengths, directions, and angles of the flap extension are isoform-specific additional features, functioning like spikes under the shoe sole, to provide auxiliary support during the motor cycle.

Although structure comparison in stalk region of DNAH1s with that of OAD isoforms reveals that axonemal dynein stalk has unique kink at the tip of CC1, it is required to confirm with high-resolution OAD structure due to its low-resolution of 8 Å (**Figure 11a**). KIH packing and heptad repeat pattern were analyzed by SOCKET2 software to identify the reason of unique kink in DNAH structure (**Figure 11b, 12b-d**). Interestingly, DNAH1s shows tighter KIH packings than that of Stalk277 despite the same registry of low affinity beta. Therefore, uniquely kinked DNAH1s CC1 helix, as indicated by lower amino acid conservation according to the ConSurf analysis, could be attributed to the tighter coiled coil packing in DNAH1s compared to Stalk277.

A difference in KIH packing in the two long coiled coils can give us a faint hint to understand the helix sliding models. It is still elusive how this conversion can occur, involving extensive rearrangement of KIH packings. A piston-like direct sliding without any structural change in helices appears to be energetically unfavorable, and conversion between α and +β registry is thought to accompany partial melting of one helix, whole unwinding/rewinding of two helices, or zippering from either end of the coiled coil, as shown in **Figure 12a**. Along with the less KIH packings in the Stalk277 structure, the fully distributed KIH packing in DNAH1s came out as the fully zipped up +β registry structure, thus completing the helix sliding zipper model (most left model in **Figure 12a**). Further experiments may be necessary to confirm whether this different packing tightness is specific to the axonemal dynein.

In summary, this study successfully determined the first atomic structure of IAD,

providing a foundation for further structural analysis of the IAD complex. Although there were only minor differences in the MTBD orientation and KIH packing, two significant features of IAD dynein were identified. These include the presence of isoform-specific flap orientation among axonemal dyneins and angular differences in domain arrangement supporting type-specific movement of axonemal and cytoplasmic dyneins. This research serves as the first step in capturing IAD MTBD, and it opens the door for further studies to accumulate more axonemal dynein MTBD structures in high resolution. This will lead to a better understanding of the different motor mechanisms between axonemal and cytoplasmic dynein. The insights gained from this work will be valuable in advancing our knowledge of dynein motor proteins and their roles in cellular functions.

Chapter 3

Triple complex of the SRS-fused human dynein and the porcine tubulin dimer with adaptor protein

3.1 Introduction

In this chapter, I focus on the motor mechanism of cytoplasmic dynein, a protein crucially involved in various neuro-diseases including lissencephaly, pachygyria, and polymicrogyria. A goal of this chapter was to understand the atomic structure of SRS-fused human cytoplasmic dynein-1, which exhibits a strong binding affinity for microtubules (α registry), both independently and in complex with porcine tubulin dimer. Although X-ray crystallography and cryo-EM structures have provided valuable information about the general architecture of the α registry structure, the specific interaction between dynein MTBD including the stalk coiled coil and microtubules at the atomic level remains poorly characterized.

Previous attempts of structural characterization of SRS-human dynein construct with the α registry, following a similar strategy as the SRS-mouse dynein construct[49], revealed complete proteolysis of the dynein region by contaminant proteases, resulting in successful crystallization of only the SRS part. To address this challenge, I have undertaken the design of three novel constructs that modify the length of the SRS region, optimizing its connecting region with the stalk region and enhancing overall stability. Successfully expressing and

purifying all three constructs, I have even obtained crystals for one of them.

In addition to the crystallization of dynein alone, I have formed the complex of SRS-dynein with the tubulin dimer to shed light on the detailed interacting mechanisms underlying dynein's motor function. To prevent microtubule dynamic polymerization, the adaptor protein D1 designed ankyrin repeat protein (DARPin) is included in the complexation process. Remarkably, I have successfully produced these triple complexes and have made significant progress towards their crystallization.

This study makes a substantial contribution to our understanding of the sample preparation of dynein at work in future analyses and holds tremendous promise for the development of therapeutic strategies targeting neuro-diseases associated with dynein dysfunction.

3.2 Materials and methods

3.2.1 SRS-fused human dynein

Cloning and Expression

The hDS2219 construct has previously been shown to be successfully expressed and purified. However, during the crystallization step, the dynein stalk region was completely cleaved off, and only the Seryl-tRNA synthetase (SRS) part was crystallized. To obtain the whole SRS-fused dynein structure, I created three novel constructs (hDS_const1-3) that modulate the SRS covering region of hDS2219. The reason for increasing Seryl-tRNA synthetase is that it has similar antiparallel helices to the dynein stalk region, and its crystal packing stability appears to be better than that of dynein. The details of the constructs are presented in **Figure 16**.

To obtain the whole SRS-fused dynein structure, I amplified the DNA that encodes a region of *Homo sapiens* cytoplasmic dynein-1 stalk with extra SRS from hDS2219. The amplified DNA fragments were cloned into the pET17b vector, which includes SRS, a TEV cleavage site following the Twin-strep tag and an ampicillin resistance gene for selection. I used the Gibson assembly method to combine the amplified DNA fragments, and the resulting plasmid was transformed into *E. coli* DH5α. After obtaining the fresh recombinant plasmid from mini-prep, I used it to transform *E. coli* BL21(DE3) competent cells for heterologous gene expression.

To initiate protein expression, a single colony of freshly transformed BL21(DE3) was inoculated into 200 mL of LB broth supplemented with 100 μg/mL ampicillin as a starter culture. Starter cultures were grown for 16 hours in a shaking incubator at 180 rpm at 310 K. For protein overexpression, 15 mL of the starter culture was used to inoculate 1.5 L of fresh

LB broth containing 100 μg/mL ampicillin. A total of 6 L of culture was incubated at 310 K, shaking at 120 rpm. Cell growth was monitored by periodically measuring the OD_{600}. Once the OD_{600} value reached 0.6-0.8, heterologous gene expression was induced by the addition of 0.5 mM IPTG, and culturing was continued overnight at 285 K. Cells were harvested by centrifugation, and the pellets were stored at 193 K until required.

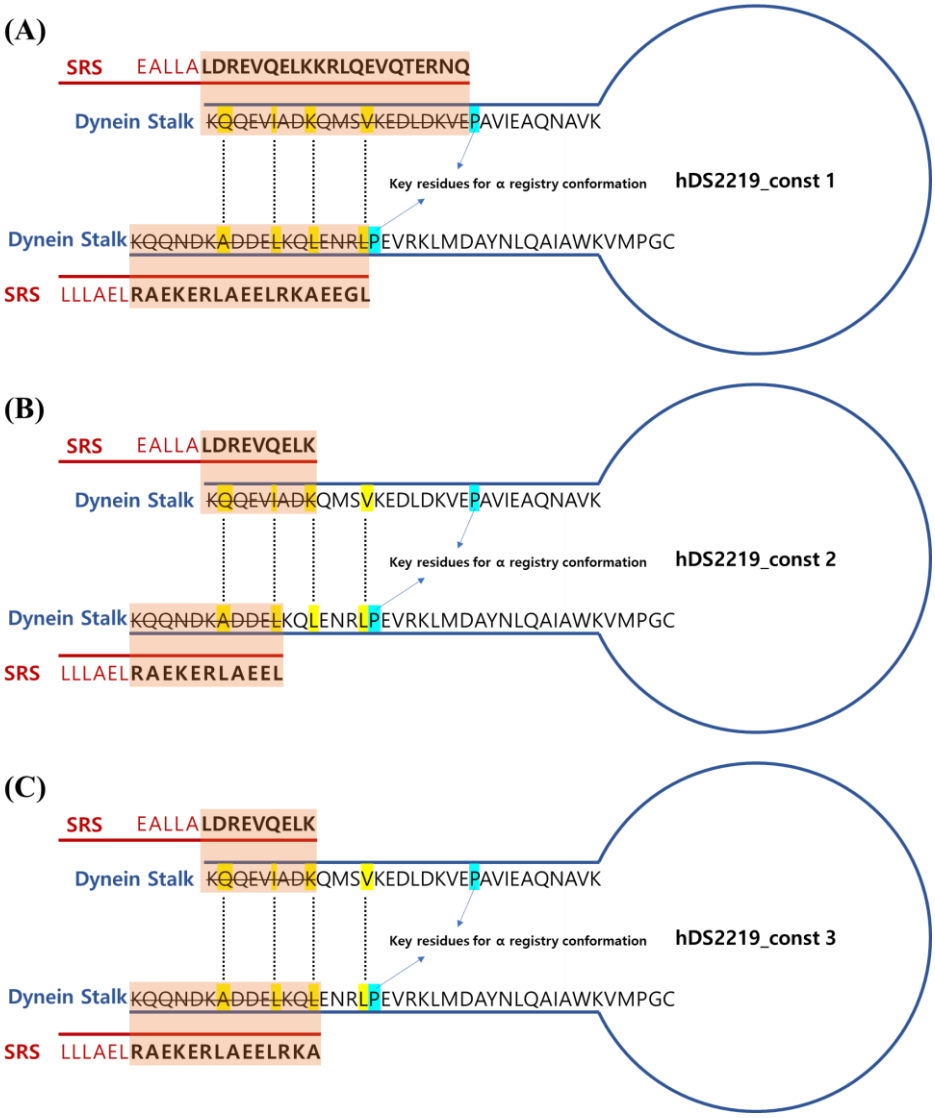

Figure 16. Schematic diagram of newly designed hDS2219 constructs

(A) hDS2219_const1 having much longer SRS helices, (B) hDS2219_const2 with less SRS helices than that of hDS2219_const1, and (C) hDS2219_const3 with the intermediate SRS helices between (A) and (B).

Purification

The frozen cell pellets were thawed and resuspended in 100 mL of Buffer W [100 mM Tris-HCl pH 8.0, 300 mM NaCl, 10 % Glycerol, 1 mM Dithiothreitol (DTT)] supplemented with two tablets of cOmplete™, EDTA-free Protease Inhibitor Cocktail (Roche). The cells were lysed by 4-5 cycles of sonication on ice, and the resultant lysate was clarified by ultracentrifugation at 200,000 × *g* for 30 minutes at 277 K. The supernatant was loaded onto a 5 mL Strep-Tactin® Superflow® high capacity FPLC column (IBA Lifesciences) that had been pre-equilibrated with 5 CV of Buffer W, at a flow rate of 5 mL/min using a peristaltic pump at 277 K. To increase the efficiency of capturing the target protein, the flow-through was recirculated into the column for 30 minutes.

The sample-loaded column was then connected to an ÄKTA FPLC (Cytiva) and washed with 20 CV of Buffer W to remove nonspecific binding proteins. The bound target protein was subsequently eluted by 20 CV Buffer E [100 mM Tris-HCl pH 8.0, 300 mM NaCl, 10 % Glycerol, 1 mM DTT, 5 mM Desthiobiotin], and the eluted samples were collected in 2 mL fractions. Sample purity was assessed by SDS-PAGE, and fractions containing the protein of interest were pooled prior to the size-exclusion chromatography step.

The protein underwent further purification via size-exclusion chromatography using a HiLoad 16/600 Superdex 200 pg column (Cytiva), which was pre-equilibrated with 1 CV of SEC buffer [20 mM Tris-HCl pH 8.0, 100 mM NaCl, 10 % Glycerol, 1 mM DTT]. Fractions containing the target protein were combined and concentrated using an Amicon Ultra-4 Centrifugal Filter Unit (10 kDa MWCO; Millipore). The protein concentration was determined using the Protein Assay Rapid Kit wako II (Fujifilm). Finally, the newly designed SRS-fused dynein proteins (hDS_const1-3) were snap-frozen in 100 uL aliquots in liquid nitrogen and stored at 193 K until further use in crystallization.

Crystallization and preliminary X-ray diffraction

The initial screening of crystallization was conducted using the sitting drop vapor diffusion method to determine the crystallization tendency of hDS_const1-3. Crystallization droplets were prepared using the mosquito LCP (stp labtech) by mixing 200 nL of protein sample dissolved in SEC buffer with an equal volume of commercially available reservoir solution from Hampton Research. The initial crystals of hDS_const3 were obtained under the condition of 0.1 M sodium malonate pH 7.0 and 12 % PEG 3350 at 293 K. Subsequently, the crystals were optimized to a cubic shape using the hanging drop vapor diffusion method under the condition of 0.15 M sodium malonate pH 7.0 and 16 % PEG 3350 at 293 K.

The crystals were briefly soaked in a cryoprotectant solution containing the crystallization buffer [30 % (v/v) glycerol, 0.15 M sodium malonate pH 7.0 and 16 % PEG 3350] and then flash frozen in liquid nitrogen. X-ray diffraction images were collected at SPring-8 (Japan) using the beamline BL44XU. Table 3 shows the related crystallographic data.

3.2.2 Porcine Tubulin

Sample preparation

Porcine brain tissue was sourced from Osaka Shokuniku Zouki (大阪食肉臓器) to obtain porcine tubulin. Porcine brain tissue was chosen as the source due to its high abundance and relatively low cost compared to other sources such as bovine brain or insect cell expression system. Additionally, porcine tubulin shares a high degree of homology with human tubulin, making it a useful model for studying the structure and function of human tubulin.

The tubulin proteins were purified using a modified version of the method described by Castoldi and Popov, 2003[50]. The purification protocol involved microtubule polymerization-depolymerization in a high-molarity buffer. As this protocol includes temperature-based experiments, it was necessary to prepare the entire stock and buffer (except the nucleoside triphosphate) in advance and store them at the required temperature. The chemical compositions and required storage temperatures are presented in **Table 2**.

The extracted porcine brains were immediately conserved in ice-cold PBS buffer and used for tubulin purification as soon as possible to maintain protein quality.

Table 2. Composition and Storage temperature of buffer and stock solutions

Buffer and stock solution	Composition	Temperature
PBS buffer	20 mM Sodium phosphate pH 7.2, 150 mM NaCl	277 K
Depolymerization buffer (DB)	50 mM MES-HCl pH 6.6, 1 mM $CaCl_2$	277 K
Final buffer (TubF)	10 mM Tris-HCl pH 8.0, 100 mM NaCl, 1 mM $MgCl_2$, 0.5 mM EGTA	277 K
High-molarity PIPES buffer (HMBP)	1 M PIPES-KOH pH 6.9, 10 mM $MgCl_2$, 20 mM EGTA	310 K
Glycerol	100 % glycerol	310 K

Purification

First, the brain tissue was cleaned of any blood clots using kitchen paper and weighed. The tissue was then transferred to a Waring blender and homogenized with Depolymerization buffer (DB) at a ratio of 1 mL per gram of tissue, using 4 rounds of 10-second homogenization at 277 K. The resulting homogenate was centrifuged at 29,000 × *g* for an hour at 277 K to separate the supernatant from the pellet.

Next, the resulting supernatant was combined with an equal volume of pre-warmed High-molarity PIPES buffer (HMPB) and anhydrous glycerol at 310 K, supplemented with a final concentration of 1.5 mM ATP and 0.5 mM GTP. The mixture was incubated in a 310 K-water bath for an hour to allow for tubulin polymerization, after which the polymerized tubulin was pelleted at 151,000 × *g* for 30 minutes at 310 K.

The resulting microtubule pellets were gently resuspended in 60 mL of cold DB using a brush and incubated for a further 30 minutes on ice. After this depolymerization step, the tubulin was centrifuged at 104,000 × *g* for 30 minutes at 277 K. The resulting tubulin supernatant was collected and subjected to another polymerization step by mixing with an equal volume of pre-warmed HMPB and anhydrous glycerol at 310 K, supplemented with a final concentration of 1.5 mM ATP and 0.5 mM GTP. The mixture was incubated in a 310 K-water bath for an hour, after which the polymerized tubulin was pelleted at 151,000 × *g* for 30 minutes at 310 K.

Following the centrifugation, the microtubule pellets were resuspended in 5 mL of cold Final buffer (TubF) and then incubated for a further 10 minutes on ice. The functional tubulin was centrifuged at 104,000 × *g* for 30 minutes at 277 K, and the resulting supernatant was collected, and the concentration measured at A_{280} using an extinction coefficient of 115,000. Finally, the purified tubulin was snap-frozen in 500 uL aliquots in liquid nitrogen and stored at 193 K until use.

3.2.3 D1 designed ankyrin repeat protein (DARPin)

Cloning and Expression

The D1 DARPin gene was artificially synthesized using the same strategy as the DARPin construct used for the kinesin-tubulin complex[51]. To express the gene, it was cloned into a pET17b vector, which includes a TEV cleavage site following the Twin-strep tag and an ampicillin resistance gene for selection. The recombinant plasmid was then used to transform *E. coli* BL21(DE3) competent cells for heterologous gene expression.

A single colony of freshly transformed BL21(DE3) cells was used to initiate protein expression by inoculating it into 200 mL of LB broth supplemented with 100 μg/mL ampicillin as a starter culture. The starter cultures were grown for 16 hours in a shaking incubator at 180 rpm at 310 K. To overexpress the protein, 15 mL of the starter culture was used to inoculate 1.5 L of fresh LB broth containing 100 μg/mL ampicillin. The total culture volume of 6 L was incubated at 310 K, shaking at 120 rpm. The growth of the cells was monitored by periodically measuring the OD_{600}. Once the OD_{600} value reached 0.6-0.8, heterologous gene expression was induced by the addition of 0.5 mM IPTG, and culturing was continued for a further 16 hours at 293 K. Finally, the cells were harvested by centrifugation and the pellets were stored at 193 K until required.

Purification

To start the purification process, the frozen cell pellets were thawed and resuspended in 100 mL of Buffer W [100 mM Tris-HCl pH 8.0, 500 mM NaCl] supplemented with two tablets of cOmplete™, EDTA-free Protease Inhibitor Cocktail (Roche). The cells were lysed by 4-5 cycles of sonication on ice, and the resultant lysate was clarified by ultracentrifugation at 200,000 × *g* for 30 minutes at 277 K.

The resulting supernatant was loaded onto a 5 mL Strep-Tactin® Superflow® high capacity FPLC column (IBA Lifesciences) that had been pre-equilibrated with 5 CV of Buffer W, at a flow rate of 5 mL/min using a peristaltic pump at 277 K. To improve the target protein's capture efficiency, the flow-through was recirculated into the column for 30 minutes.

The column with the loaded sample was then connected to an ÄKTA FPLC (Cytiva) and washed with 20 CV of Buffer W to remove nonspecific binding proteins. The target protein was subsequently eluted by 20 CV Buffer E [100 mM Tris-HCl pH 8.0, 500 mM NaCl, 5 mM Desthiobiotin], and the eluted samples were collected in 2 mL fractions. The purity of the samples was assessed by SDS-PAGE, and fractions containing the protein of interest were pooled prior to the size-exclusion chromatography step.

The protein was further purified using size-exclusion chromatography with a HiLoad 16/600 Superdex 75 pg column (Cytiva) that had been pre-equilibrated with 1 CV of SEC buffer [10 mM Tris-HCl pH 8.0, 100 mM NaCl]. Fractions containing the target protein were combined and concentrated using an Amicon Ultra-4 Centrifugal Filter Unit (10 kDa MWCO; Millipore). The protein concentration was determined using the Protein Assay Rapid Kit wako II (Fujifilm). The purified D1 DARPins were snap-frozen in 100 µL aliquots in liquid nitrogen and stored at 193 K until needed for complex formation.

3.2.4 Triple complex

Purification

The porcine tubulin, hDS_const3, and D1 DARPin were mixed in a 1:1.5:1.5 molar ratio and incubated for 30 minutes at 277K to allow for the formation of the triple complex. The mixture was further purified using size-exclusion chromatography with a Superdex® 200 Increase 10/300 GL (Cytiva) pre-equilibrated with 1 CV of SEC buffer [10 mM Tris-HCl pH 8.0, 100 mM NaCl, 1 mM $MgCl_2$, 0.5 mM EGTA]. Fractions containing the complexed protein were combined and concentrated using an Amicon Ultra-4 Centrifugal Filter Unit (30 kDa MWCO; Millipore). The final protein concentration was determined using the Protein Assay Rapid Kit wako II (Fujifilm), and the sample was directly used for crystallization.

Crystallization and preliminary X-ray diffraction

To determine the crystallization tendency of the triple complex, initial screening was conducted using the sitting drop vapor diffusion method. Crystallization droplets were prepared using the mosquito LCP (STP Labtech) by mixing 200 nL of the protein sample dissolved in SEC buffer with an equal volume of commercially available reservoir solution from Hampton Research.

The obtained crystals were briefly soaked in a cryoprotectant solution containing the crystallization buffer and 30 % (v/v) glycerol, followed by flash freezing in liquid nitrogen. X-ray diffraction images were collected at SPring-8 (Japan) using the beamline BL44XU.

3.3 Results

3.3.1 SRS-fused human dynein

Cloning and Expression

To determine the optimal overexpression conditions for hDS_consts, small-scale expression tests were performed using high (310 K) and low (291 K) induction temperatures in different expression cells [BL21(DE3), BL21(DE3) codon plus, Rosetta2] with 0.5 mM IPTG induction. From the screening, I found that all three constructs displayed a similar trend, with lower induction temperatures resulting in higher expression levels. Based on these findings, I scaled up the culture to 6 L with 0.5 mM IPTG induction at 18°C overnight. As a result, three new constructs of SRS-fused dynein stalk (hDS_const1-3) were successfully overexpressed in *E. coli* BL21(DE3) cells **(Figure 17)** and subjected to a two-step purification process involving affinity and size-exclusion chromatography.

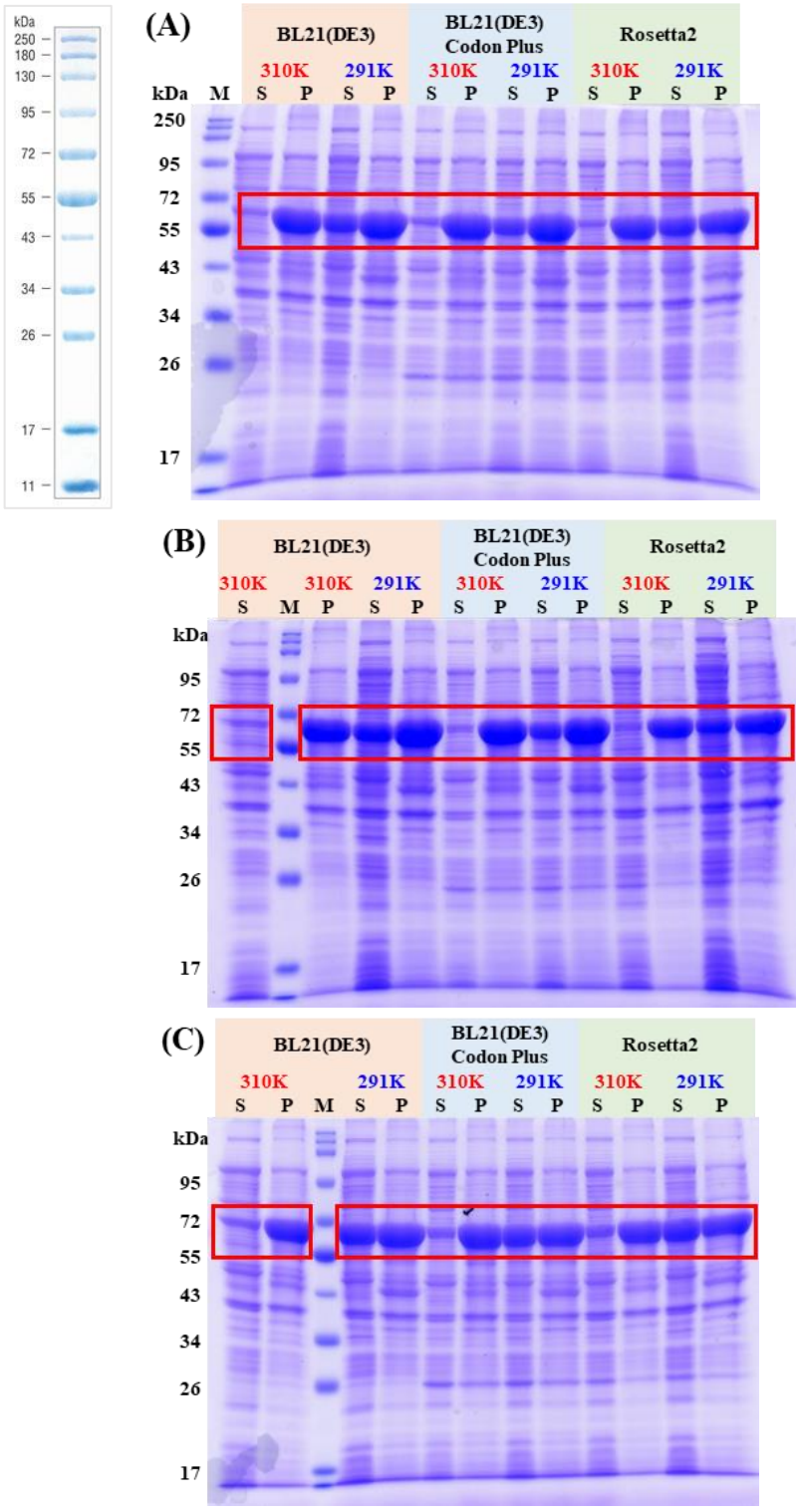

Figure 17. Expression test results of hDS_const1-3

Expression test results of (A) hDS_const1, (B) hDS_const2 and (C) hDS_const3. The top-left image displays the entire size of the protein molecular weight marker.

Information for the loaded fractions includes: M: Molecular weight marker, S: supernatant, P: pellet. The overexpressed target proteins are indicated in the red box.

Purification

For the first step of hDS_const purification, the cell lysate was loaded onto a 20 mL Strep-Tactin® Sepharose® resin (IBA Lifesciences) after cell lysis. After removing non-specifically bound proteins by washing the resin with 5 CV of Buffer W, target proteins were eluted with 5 mM desthiobiotin using a peristaltic pump. Fractions of elution volume ranging from 5 to 65 mL were collected in 5 mL increments and analyzed through SDS-PAGE. The results confirmed that the scaled-up expression followed the same trend observed in the small-scale solubility and expression level **(Figure 18)**. Fractions containing proteins of interest were then collected for further purification.

To ensure that the maximum injection volume for gel filtration was not exceeded, the sample was concentrated to a volume of 1 mL and applied onto a pre-equilibrated HiLoad 16/600 Superdex 200 pg column (Cytiva) with SEC buffer. Following elution, peak fractions were collected and analyzed through SDS-PAGE **(Figure 19-21)**. Although contaminant proteins were still present after the two-step purification, the purity of the target protein had significantly improved compared to the previous step. The purest hDS_const elution fractions were then concentrated up to 15 mg/mL in preparation for the crystallization step.

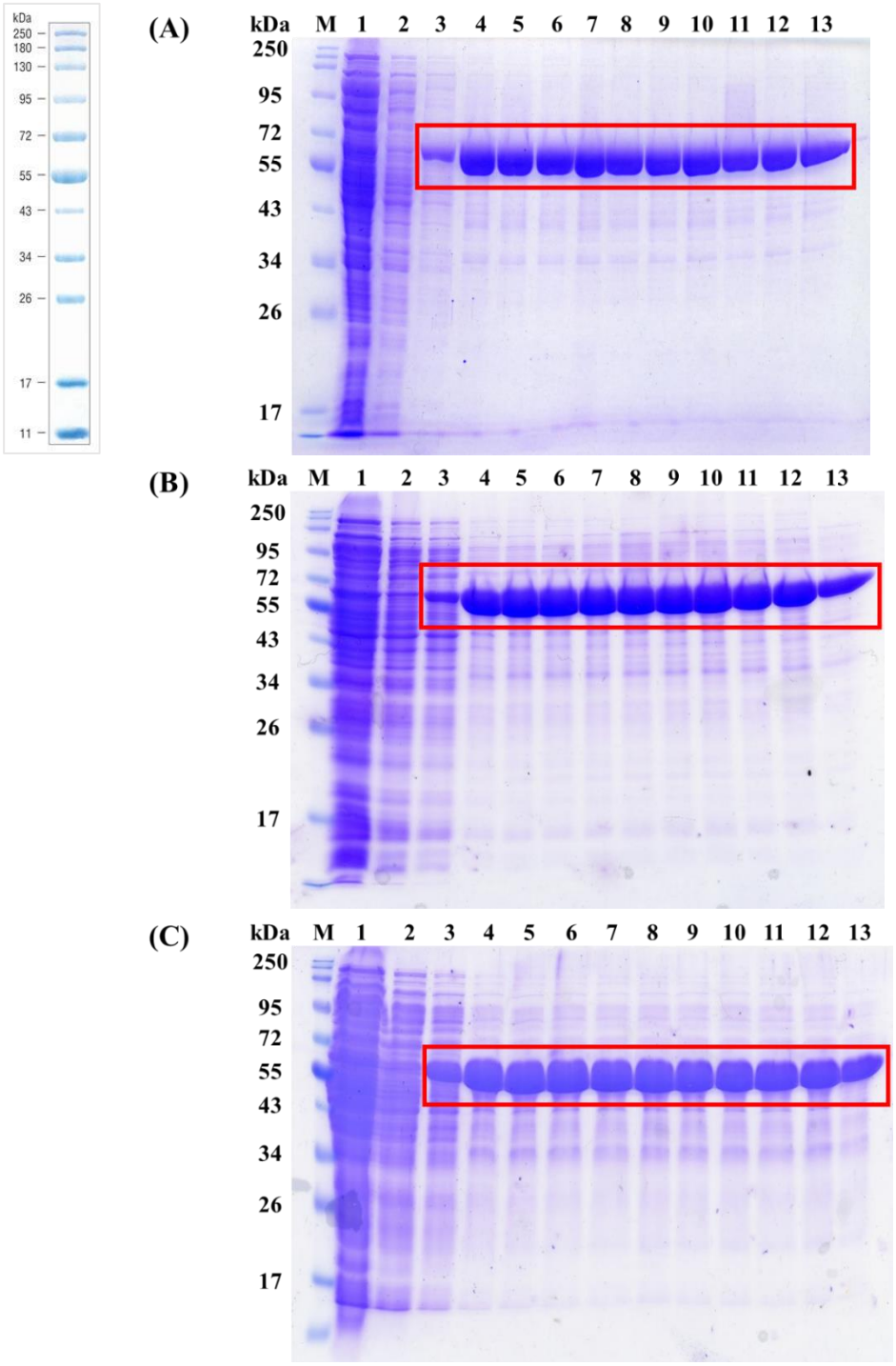

Figure 18. Affinity chromatography result of hDS_const1-3

Affinity chromatography results of (A) hDS_const1, (B) hDS_const2 and (C) hDS_const3. The top-left image shows the entire size of the protein molecular weight marker. SDS-PAGE loaded fractions include: M: Molecular weight marker, Lane 1: Flow-through, Lane 2: Wash, Lane 3-13: Elution fractions. The eluted target proteins are marked in the red box.

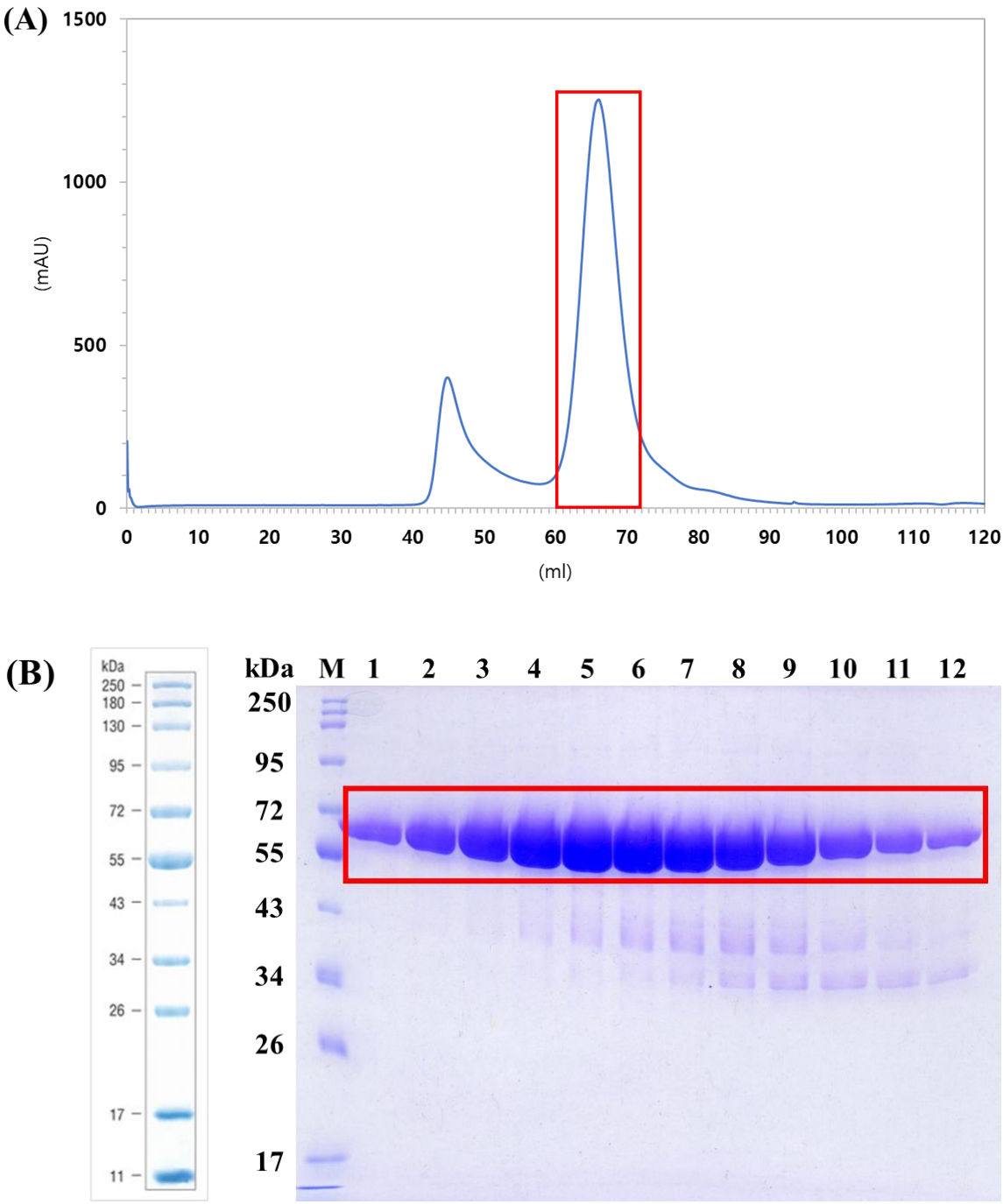

Figure 19. Size-exclusion chromatography result of hDS_const1

(A) Elution profile of gel filtration with UV trace at 280 nm (blue). hDS_const1 eluted with a peak at fractions between 59 and 79 mL.

(B) SDS-PAGE result of SEC. The left-side image illustrates the entire size of the protein molecular weight marker. Information for the loaded fractions is as follows: M: Molecular weight marker, Lane 1-12: 1 mL elution fractions from 60-72 mL. Target proteins are marked in the red box.

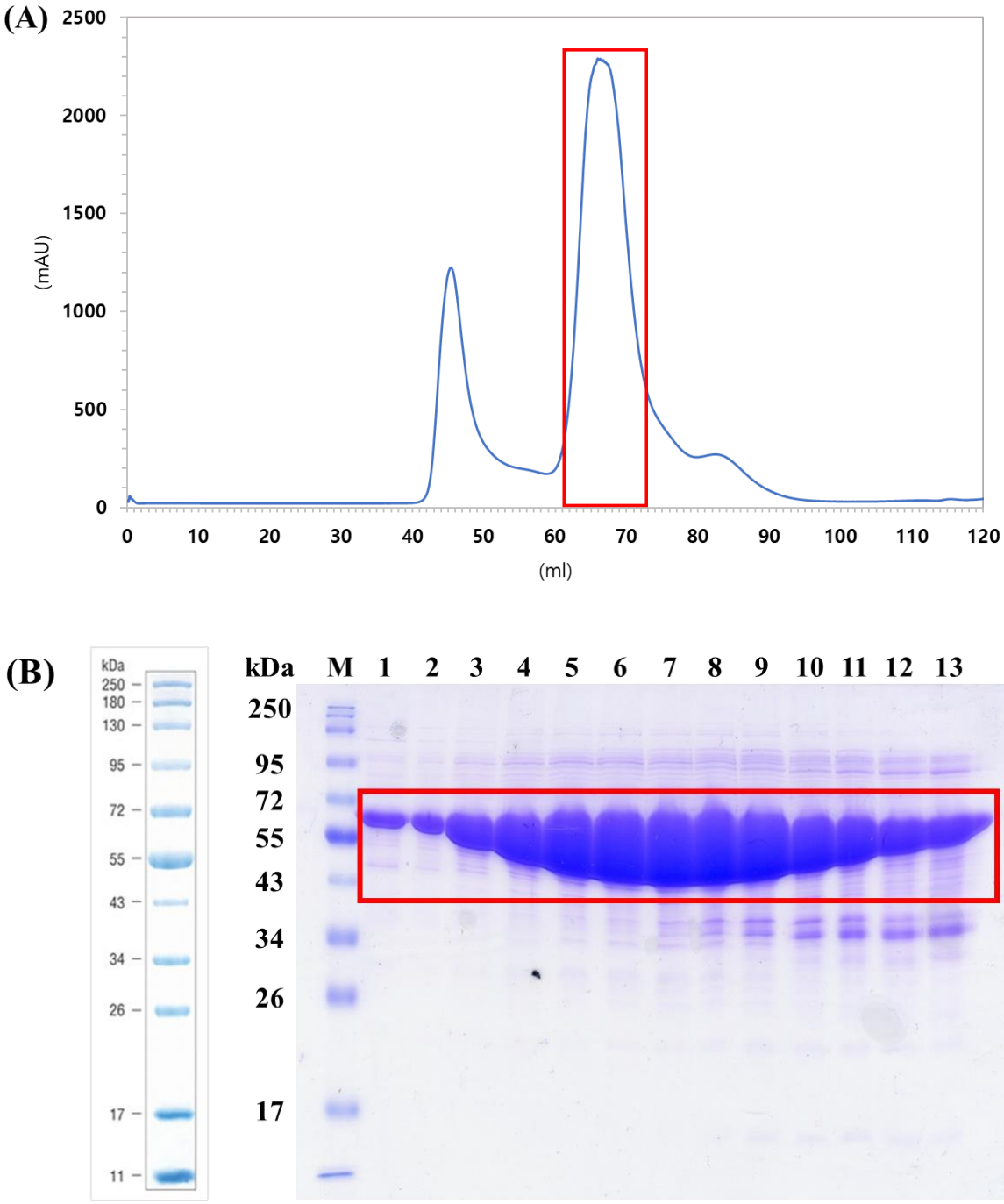

Figure 20. Size-exclusion chromatography result of hDS_const2

(A) Gel filtration elution profile with UV trace at 280 nm (blue) showing hDS_const2 eluting as a peak in fractions ranging from 59 to 79 mL.

(B) SDS-PAGE analysis of hDS_const2 after size-exclusion chromatography. The image on the left displays the entire protein molecular weight marker. Loaded fractions are as follows: M: Molecular weight marker, Lane 1-13: 1 mL elution fractions from 61-74 mL. The target proteins are highlighted by the red box.

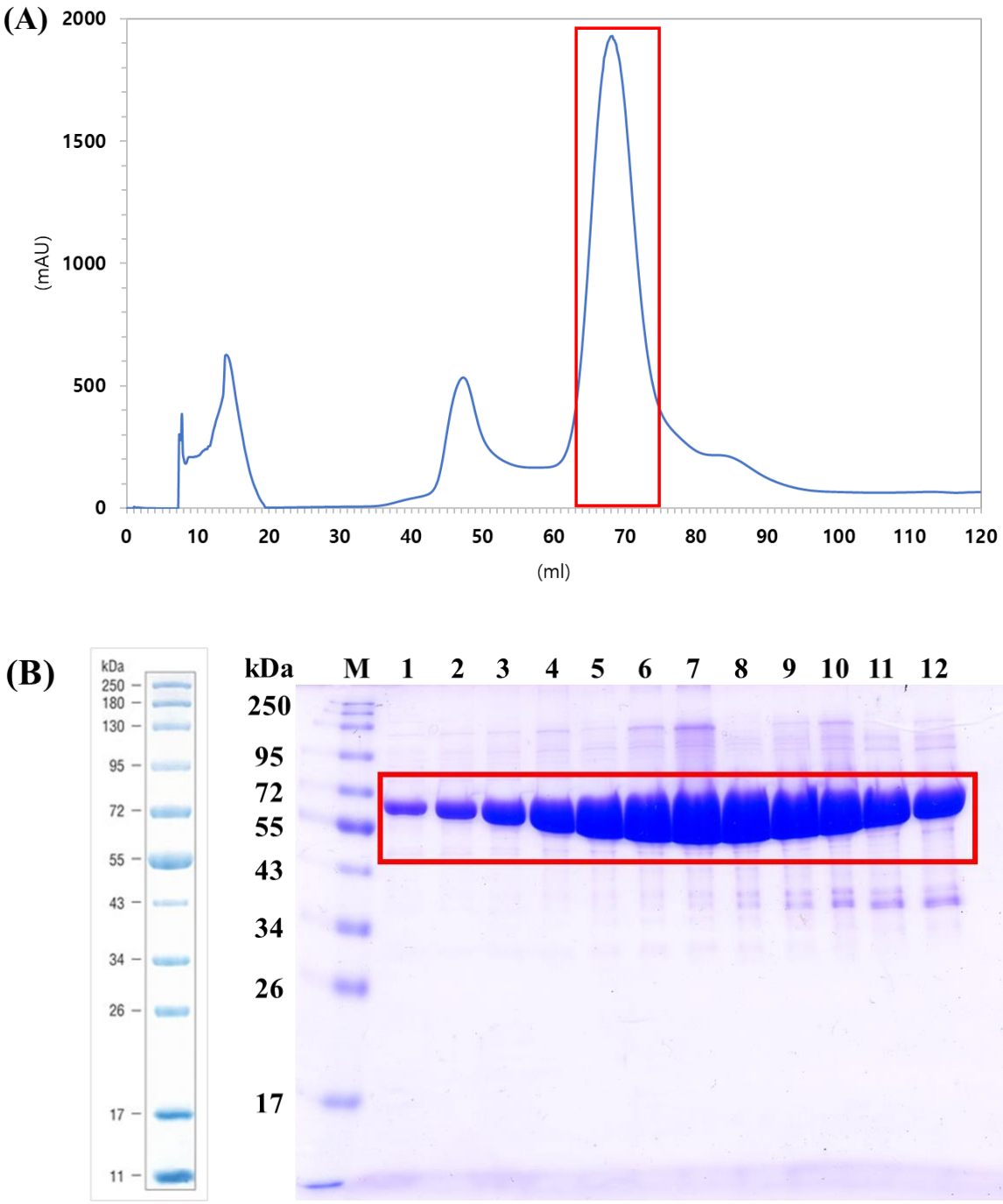

Figure 21. Size-exclusion chromatography result of hDS_const3

(A) Elution profile of gel filtration with UV trace at 280 nm (blue). hDS_const3 w as eluted with a peak observed in fractions ranging from 60 to 81 mL.

(B) SDS-PAGE result of SEC. The image on the left shows the entire protein mole cular weight marker. Loaded fractions are as follows:

M: Molecular weight marker, Lane 1-12: 1 mL elution fractions from 63-75 mL. The target proteins are indicated by the red box.

Crystallization and preliminary X-ray diffraction experiment

Initial crystallization screening was conducted using all three constructs of hD S_const1-3, following the protocol described in the Materials and Methods section. Ho wever, only the hDS_const3 sample produced clumpy grain-shaped crystals under the condition of 0.1 M sodium malonate pH 7.0 and 12% PEG 3350 at 293 K after 18 hours **(Figure 22a)**. To obtain high-quality crystals suitable for X-ray diffraction, cryst allization condition was optimized by refining the initial conditions. As a result, cubic -shaped crystals were obtained after 2 weeks under the condition of 0.15 M sodium malonate pH 7.0 and 16% PEG 3350 at 293 K **(Figure 22b)**.

X-ray diffraction data were collected at the BL44XU beamline of SPring-8 in Japan. The highest resolution achieved was 3.2 Å **(Figure 23a, Table 3)**. However, upon examining the electron density map, it was observed that the dynein part exhibited significantly poorer electron density compared to the SRS part **(Figure 23b)**. This raised the suspicion that the produced crystals might have undergone proteolysis, resulting in the crystallization of only the SRS part. To confirm this, several crystals were collected and loaded onto an SDS-PAGE gel. The results revealed no bands detected below 55 kDa, confirming that hDS_const3 was not cleaved **(Figure 23c)**.

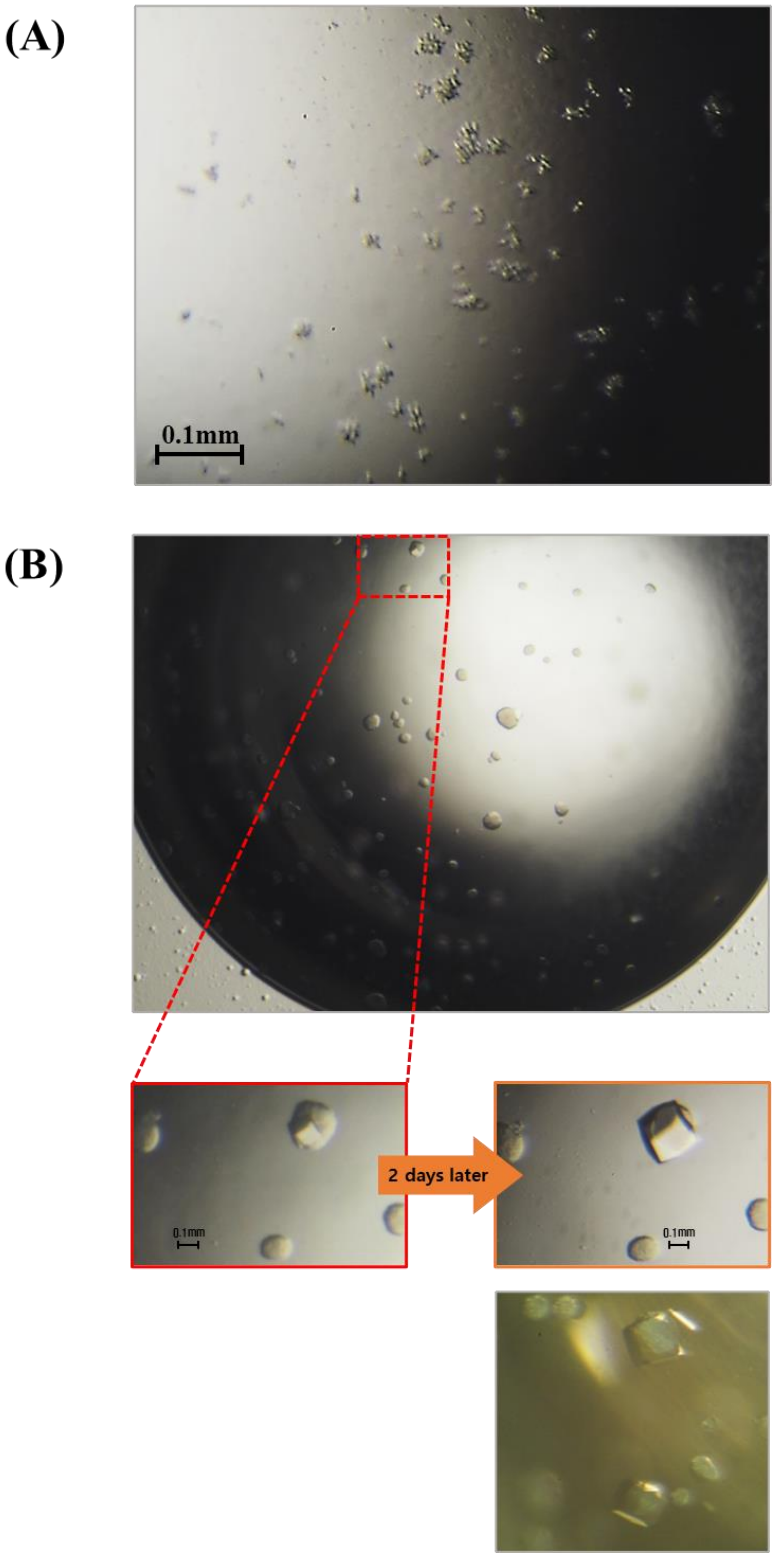

Figure 22. Crystals of hDS_const3

(A) Initial clumpy grain-shaped crystals of hDS_const3.

(B) Agglomerated protein precipitates formed initially, which subsequently led to the growth of cubic crystals from the precipitate.

Table 3. Data collection statistics

Data Collection	*hDS_const3*
Beamline	SPring-8 BL44XU
Wavelength (Å)	0.899995
Resolution range(Å)	47.05 - 3.189 (3.303 - 3.189)
Space group	$P3_121$
Unit cell (*a*, *b*, *c*/Å, α, β, γ/°)	149.016 149.016 137.522 90 90 120
Total reflections	307805
Unique reflections	29792 (2914)
Redundancy	10.3(9.7)
Completeness (%)	99.51 (99.11)
Mean I/sigma(I)	12.42(1.03)
Wilson B-factor (Å^2)	114.57
R-meas	0.134(2.01)
CC1/2	99.9(71.5)

Statistics for the highest-resolution shell are shown in parentheses

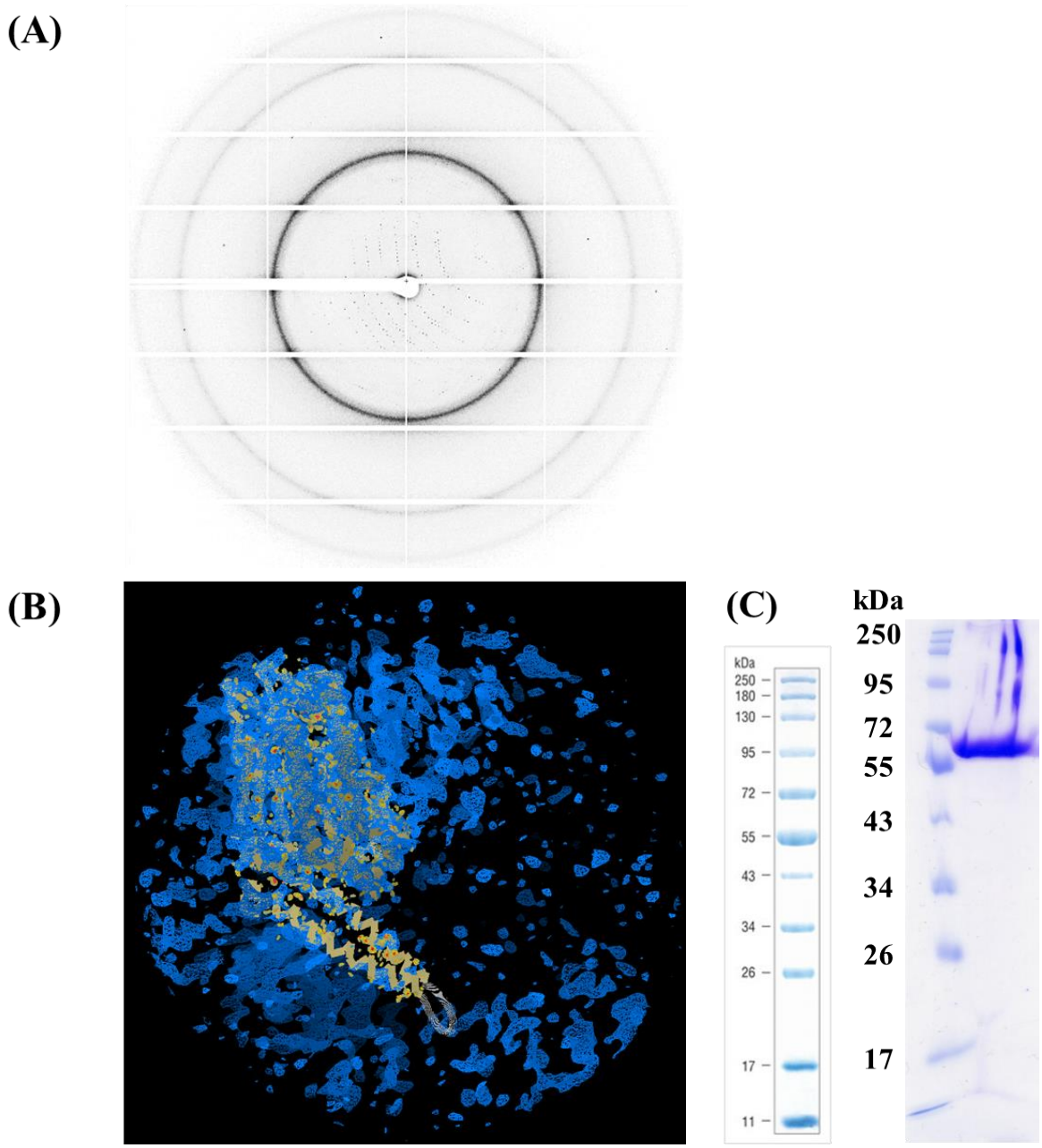

Figure 23. Preliminary X-ray diffraction and SDS-PAGE analysis of hDS_const3 crystals

(A) X-ray diffraction image of the hDS_const3 crystal.

(B) Electron density map after phase determination showing poor electron density around the dynein region compared to the SRS part.

(C) The left-side image illustrates the complete protein molecular weight marker, whi le the right side presents the SDS-PAGE analysis of hDS_const3 crystals.

3.3.2 Triple complex

Sample preparation

Both porcine tubulin and D1 DARPin were successfully purified following a previously established protocol. SDS-PAGE analysis of the tubulin purification confirmed a significant improvement in purity after repeated polymerization-depolymerization using high-molarity PIPES and MES buffer **(Figure 24)**. Although some contaminant proteins persisted after the two-step chromatography of D1 DARPin, the purity of the target protein notably improved compared to the previous stage. The purest elution fractions of D1 DARPin were subsequently concentrated to a concentration of up to 15 mg/mL, preparing them for the subsequent complexation step **(Figure 25, 26)**.

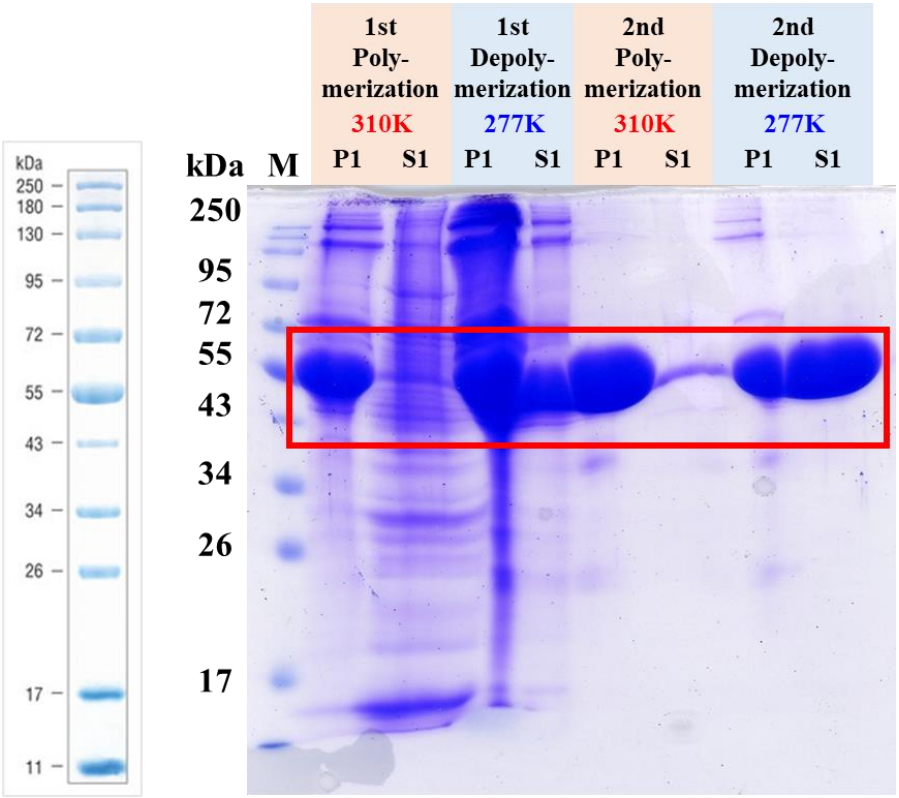

Figure 24. SDS-PAGE analysis of porcine tubulin purification

The image on the left shows the entire protein molecular weight marker. SDS-PAGE results demonstrate the extraction of tubulin from pig brain using a two-cycle polymerization and depolymerization method. The target proteins are highlighted in the red box.

Details of the loaded fractions are as follows: M: molecular weight marker S: supernatant P: pellet

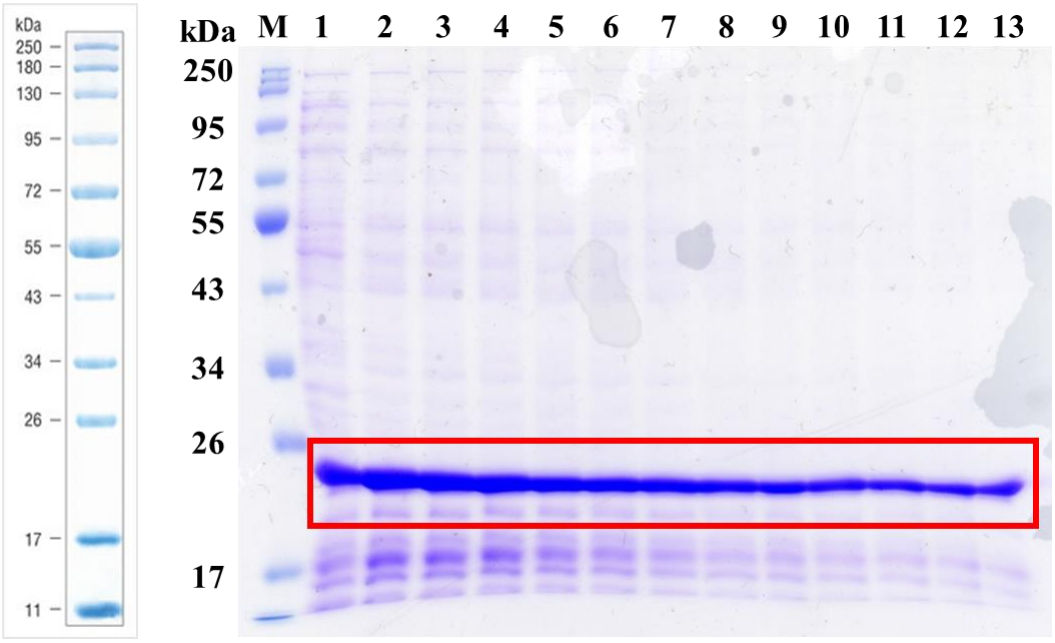

Figure 25. Affinity chromatography result of D1 DARPin

SDS-PAGE analysis of D1 DARPin. The left-side image displays the full protein molecular weight marker. SDS-PAGE loaded fractions consist of: M: Molecular weight marker, Lane 1-13: Elution fractions. The eluted target proteins are highlighted in the red box.

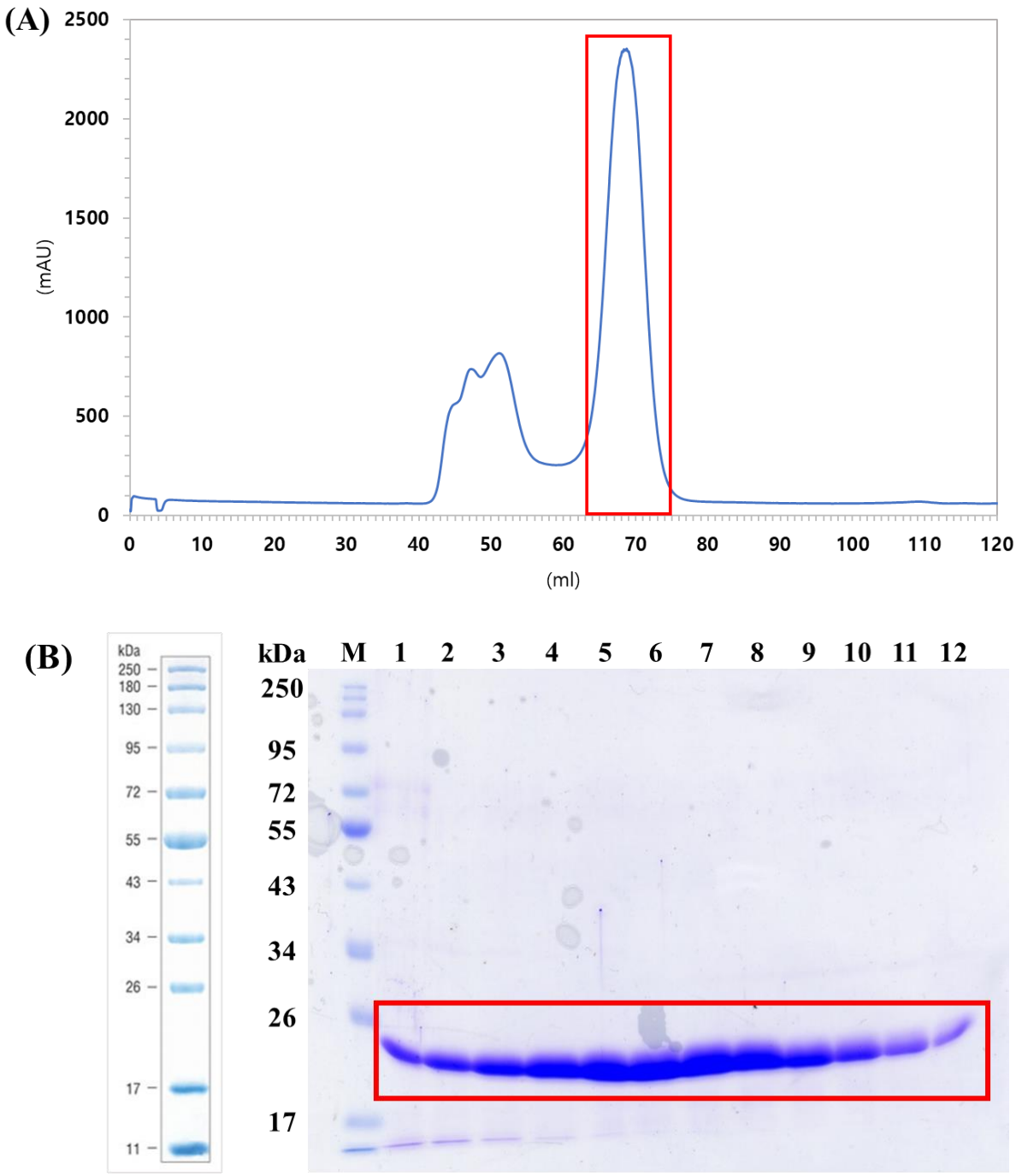

Figure 26. Size-exclusion chromatography result of D1 DARPin

(A) Gel filtration elution profile with UV trace at 280 nm (blue). D1 DARPin was eluted with a peak at fractions between 60 and 76 mL.

(B) SDS-PAGE analysis of SEC. The left-side image displays the full protein molecular weight marker. Loaded fractions are as follows: M: Molecular weight marker, Lane 1-12: 1 mL elution fractions from 63-75 mL. The target proteins are marked in the red box.

Complex formation

Although the ideal binding ratio for complex formation was 1:1:1, a 1.5-fold excess of dynein and D1 DARPin was employed compared to tubulin. This approach aimed to enhance the disassembly of the microtubule by selectively capping the D1 DARPin to the β-tubulin and increase the probability of dynein binding. After incubating the protein mixture at 277 K for 30 minutes, it was loaded onto a pre-equilibrated Superdex® 200 Increase 10/300 GL column (Cytiva) with SEC buffer. The elution profile showed two distinct peaks at 13 to 14 mL and 15.5 to 17.5 mL **(Figure 27a)**. SDS-PAGE analysis of the peak fractions revealed that the first peak fractions contained the triple complexed protein, while the second peak contained the remaining D1 DARPin **(Figure 27b)**. The fractions containing the complexed protein were combined and concentrated to a concentration of 12 mg/mL in preparation for the subsequent crystallization step.

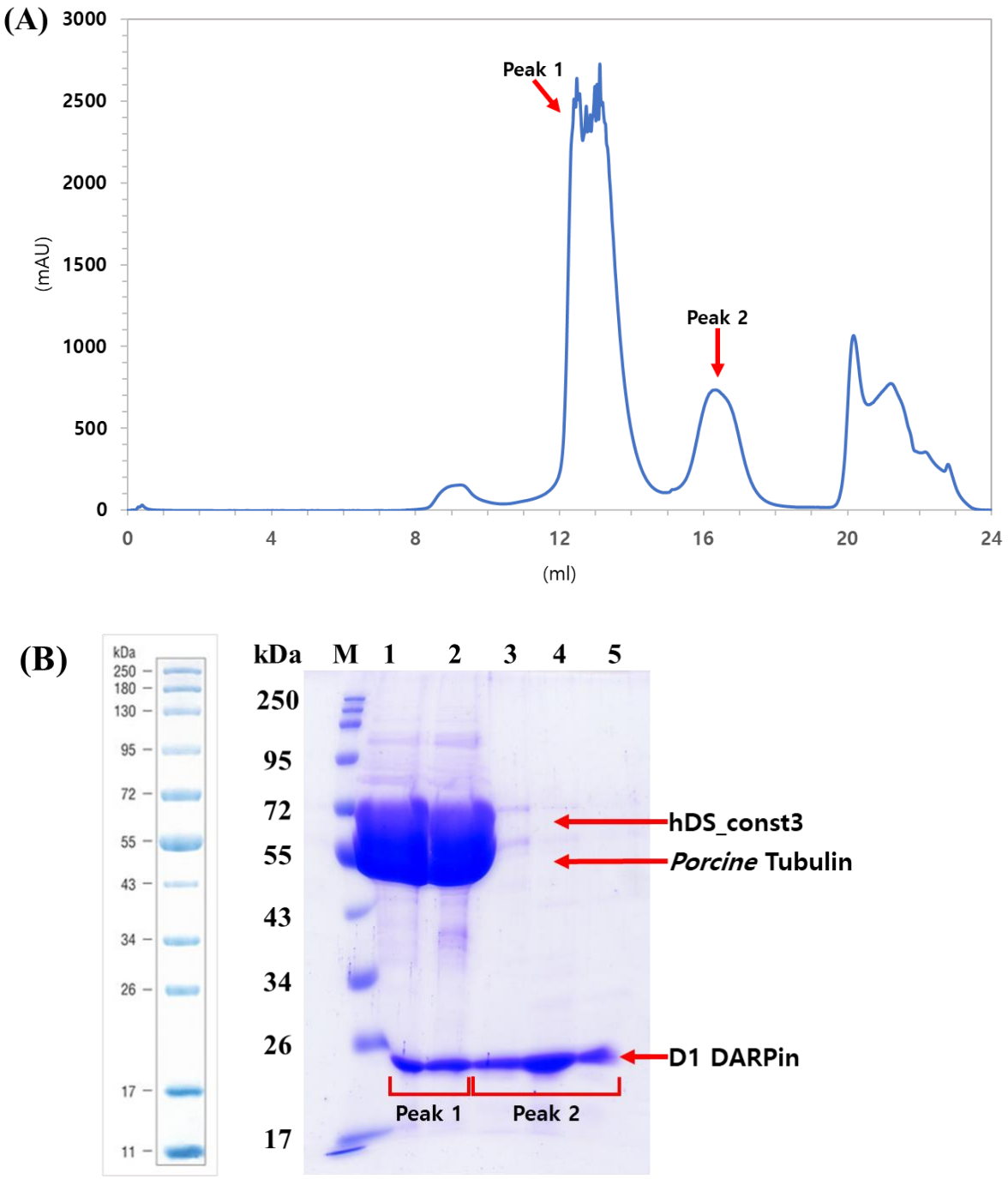

Figure 27. Size-exclusion chromatography result of triple complex

(A) Gel filtration elution profile with UV trace at 280 nm (blue). The triple complexed proteins were eluted with a peak at fractions between 12 and 14 mL.

(B) SDS-PAGE analysis of SEC. The left-side image shows the entire protein molecular weight marker. Loaded fractions are as follows: M: Molecular weight marker, Lane 1-5: 1 mL elution fractions from 12-17 mL. The target proteins are indicated in the red box.

Crystallization and preliminary X-ray diffraction experiment

The initial crystals were obtained in a thin plate shape under the conditions of 10% (v/v) MPD, 100 mM Bicine/Sodium hydroxide pH 9.0, and 40% (v/v) PEG 400, 0.1 M Tris pH 8.5, 0.2 M Lithium sulfate.

To improve the crystal quality for subsequent X-ray diffraction experiments, the crystal conditions were further refined from the initial conditions. By adjusting the conditions to 40% (v/v) MPD, 100 mM Bicine/Sodium hydroxide pH 8.5, and 50% (v/v) PEG 400, 0.1 M Tris pH 8.5, 0.2 M Lithium sulfate, thin plate shaped crystals were successfully optimized, resulting in improved thickness and size **(Figure 28)**.

Optimized crystals were collected and utilized for X-ray diffraction experiments at the BL44XU beamline of SPring-8 in Japan. However, the obtained diffraction patterns indicated that additional optimization is required to determine the atomic interaction between the dynein MTBD and tubulin dimer.

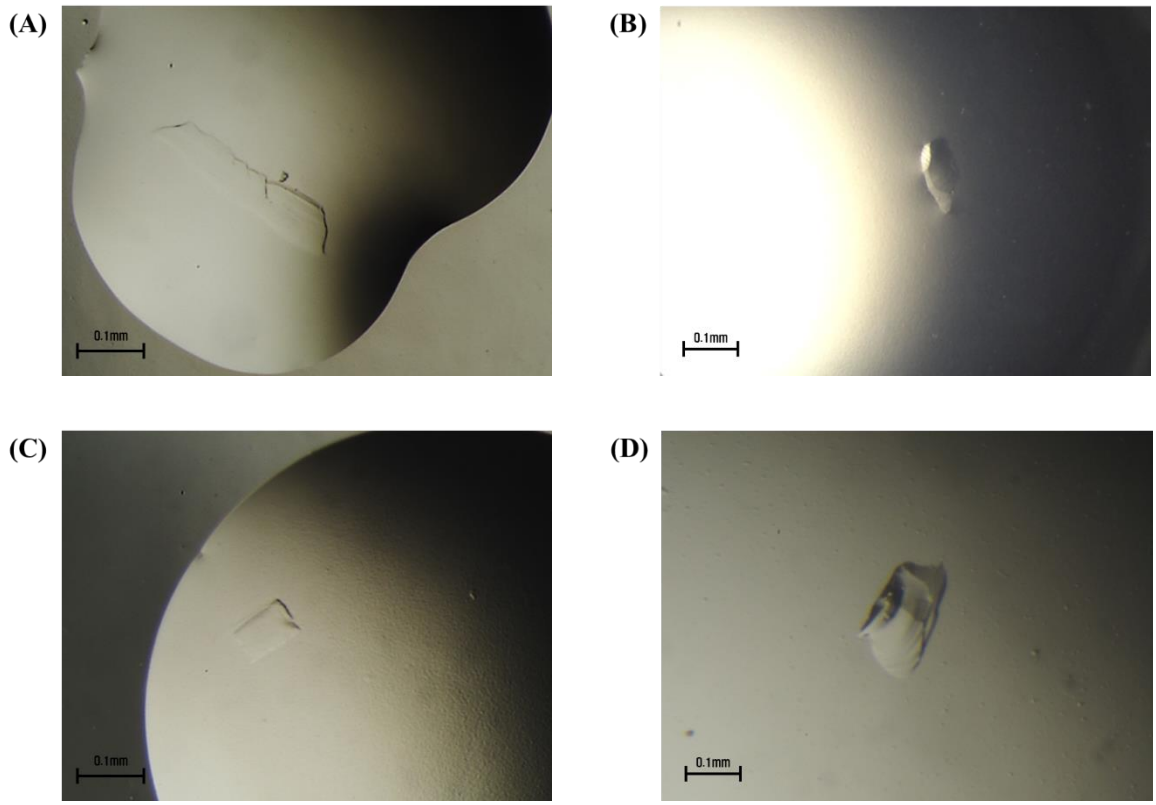

Figure 28. Crystallization of Triple complex

(A) Initial crystals in a thin plate shape under the condition of 10% (v/v) MPD, 100 mM Bicine/Sodium hydroxide pH 9.0.

(B) Optimized crystal obtained under the condition of 40% (v/v) MPD, 100 mM Bicine/Sodium hydroxide pH 8.5.

(C) Initial crystals in a thin plate shape under the condition of 40% (v/v) PEG 400, 0.1 M Tris pH 8.5, 0.2 M Lithium sulfate.

(D) Optimized crystal obtained under the condition of 50% (v/v) PEG 400, 0.1 M Tris pH 8.5, 0.2 M Lithium sulfate.

3.4 Discussion

Similar to the inner- or outer-arm axonemal dynein, structural information of the cytoplasmic dynein MTBD in high-affinity α registry conformation is very limited compared to the low-affinity +β registry. Currently available structures obtained through X-ray crystallography and cryo-EM techniques in Protein Data Bank, either exhibit very weak electron density (PDB ID: 6KIO, 6KIQ) or are missing the region entirely (PDB ID: 3VKG). To balance this knowledge gap, I prompted an investigation into a triple complex of the SRS-fused dynein and the porcine tubulin dimer with adaptor protein.

In terms of my experimental progress, I successfully generated the three essential proteins required for the triple complex: SRS-fused human dynein, porcine tubulin, and D1 DARPin. Fortunately, my efforts to assemble a triple complex comprising SRS-fused human dynein, porcine tubulin, and D1 DARPin were fruitful. However, I encountered an unexpected challenge related to its stability, which ultimately posed difficulties in achieving crystallization.

Despite these setbacks, my triple complex design offers valuable insights for potential improvements rather than being considered a complete failure. To enhance the stability of the triple complex, my next approach involved the inclusion of She1 regulatory protein known as retaining dynein-microtubule interaction[52]. However, attempts to obtain soluble She1 using the *E. coli* expression system were unsuccessful. Moving forward, I anticipate that further research on the quaternary complex, incorporating She1 expressed in insect cells (following the approach described in Ecklund et al., 2017), will provide valuable information regarding the dynein-microtubule interaction, deepening our understanding of their dynamic interplay.

The SRS-dynein crystal exhibited diffraction up to a resolution of 3.2 Å, indicating sufficient crystal quality for model building. However, upon examining the electron density map, I observed a lack of density corresponding to the dynein region. This raised concerns

about potential proteolysis of the dynein part, similar to what happened in the original construct (following the strategy of SRS-fused mouse dynein). To address this issue, I conducted SDS-PAGE analysis, which confirmed that no cleavage had occurred. To enhance the crystal quality and obtain higher resolution X-ray diffraction data, I propose employing a similar strategy as suggested for the triple complex. Addition of She1 to the SRS-dynein complex can potentially increase stability and improve the homogeneity of the protein sample. This approach holds promise for enhancing the crystal quality and facilitating the determination of a more detailed and accurate structure of SRS-fused human dynein in the state of high affinity for the microtubule. By implementing this strategy, I anticipate obtaining improved insights into the molecular interactions and mechanisms underlying the function of dynein.

In conclusion, my study has provided significant improvement in the sample preparation of SRS-fused human dynein, porcine tubulin, and D1 DARPin. However, it has also highlighted the inherent challenges associated with investigating complex protein interactions. Moving forward, future studies should aim to develop innovative techniques and approaches to overcome these challenges, allowing for the formation of more stable protein complexes. By doing so, I can further deepen our understanding of the underlying mechanisms governing the function of these proteins and their intricate interactions.

Chapter 4

Conclusion

The research presented in this thesis aimed to advance our understanding of dynein motors, which play critical roles in various biological processes. While structural studies on dyneins have been conducted using different techniques, few projects have investigated both cytoplasmic and axonal dyneins comprehensively. In this study, I had the opportunity to address this gap and provide a comprehensive analysis.

In Chapter 2, I focused on investigating the structural characteristics of axonemal dynein, which has received less attention compared to cytoplasmic dynein when I started this project. Previous structural information was primarily limited to cytoplasmic dynein, leaving the inner-arm dynein largely unexplored, except for truncated MTBD structures. I successfully determined the X-ray crystal structure of DNAH1s, which provided the first atomic-level structure of the inner-arm dynein stalk with its long coiled coil helices. My analysis revealed a slight kink in the CC1 helix and a unique flap motif in the MTBD of DNAH1s. I proposed a "spike shoes model" to explain the distinct flap orientation and its role in cilia and flagella beating. Furthermore, I identified angular differences in the relative domain arrangement of the MTBD to the coiled coil between axonemal and cytoplasmic dyneins, indicating their distinct functions and cellular localizations.

In Chapter 3, I focused on obtaining structural information on the high-affinity α registry conformation of cytoplasmic dynein MTBD. Existing structures in the Protein Data Bank lacked sufficient electron density or entirely missed this region. To address this limitation, I attempted to produce a triple complex comprising SRS-fused human dynein, porcine tubulin,

and D1 DARPin. Although the stability and crystallization of the complex posed challenges, my design offers valuable insights for potential improvements. I also explored the inclusion of the She1 regulatory protein to enhance the stability of the triple complex but obtaining soluble She1 using the *E. coli* expression system was unsuccessful. A future approach may involve using She1 expressed in insect cells to form a quaternary complex, which will deepen our understanding of the dynamic interplay between dynein and microtubules.

Also, analyzing the SRS-dynein only crystal, I obtained an X-ray diffraction data set up to a resolution of 3.2 Å, indicating sufficient crystal quality for model building. However, the obtained electron density revealed a lack of density corresponding to the dynein region. SDS-PAGE analysis confirmed no cleavage had occurred but probably the corresponding dynein part are structurally too mobile to give an interpretable electron density. To enhance crystal quality and resolution, I propose the formation of a complex with She1, as it has the potential to enhance structural stability and homogeneity. This approach holds promise for obtaining a more detailed and accurate structure of SRS-fused human dynein.

In conclusion, this PhD project successfully elucidated the first atomic structure of the inner-arm dynein stalk, providing insights into isoform-specific flap regions and angular differences in the MTBD arrangement between axonemal and cytoplasmic dyneins. Furthermore, my research on SRS-fused human dynein, porcine tubulin, and D1 DARPin revealed challenges associated with investigating complex protein interactions. To overcome these challenges, future studies should focus on developing innovative techniques that enable stable protein complex formation, allowing for a deeper understanding of the mechanisms regulating the function and interactions of dynein motors.

References

1. Fletcher DA, Mullins RD (2010) Cell mechanics and the cytoskeleton. *Nature* 463:485–492. Available from: https://doi.org/10.1038/nature08908

2. Howard J, Clark RL (2002) Mechanics of motor proteins and the cytoskeleton. *Appl. Mech. Rev.* 55:B39–B39. Available from: https://doi.org/10.1115/1.1451234

3. Vale RD (2003) The molecular motor toolbox for intracellular transport. *Cell* 112:467–480. Available from: https://doi.org/10.1016/S0092-8674(03)00111-9

4. Mallik R, Gross SP (2004) Molecular motors: Strategies to get along. *Current Biology 14* R971–R982. Available from: 10.1016/j.cub.2004.10.046

5. King SM (2000) The dynein microtubule motor. *Biochimica et Biophysica Acta (BBA) - Molecular Cell Research* 1496:60–75.
Available from: https://doi.org/10.1016/S0167-4889(00)00009-4

6. Mitchison T, Kirschner M (1984) Microtubule assembly nucleated by isolated centrosomes. *Nature* 312:232–237. Available from: https://doi.org/10.1038/312232a0

7. Fuchs E, Cleveland DW (1998) A structural scaffolding of intermediate filaments in health and disease. *Science* 279:514–519. Available from: 10.1126/science.279.5350.514

8. Dominguez R (2009) Actin filament nucleation and elongation factors–structure–function relationships. *Crit Rev Biochem Mol Biol* 44:351–366.
Available from: https://doi.org/10.3109/10409230903277340

9. Koonce MP, Grissom PM, Lyon M, Pope T, Mcintosh JR (1994) Molecular characterization of a cytoplasmic dynein from *Dictyostelium*. *Journal of Eukaryotic Microbiology* 41:645–651. Available from: https://doi.org/10.1111/j.1550-7408.1994.tb01528.x

10. Vallee RB, Williams JC, Varma D, Barnhart LE (2004) Dynein: An ancient motor protein involved in multiple modes of transport. *J Neurobiol* 58:189–200.
Available from: https://doi.org/10.1002/neu.10314

11. Howell BJ, McEwen BF, Canman JC, Hoffman DB, Farrar EM, Rieder CL, Salmon ED (2001) Cytoplasmic dynein/dynactin drives kinetochore protein transport to the spindle poles and has a role in mitotic spindle checkpoint inactivation. *Journal of Cell Biology* 155:1159–1172. Available from: https://doi.org/10.1083/jcb.200105093

12. Gibbons IR, Rowe AJ (1965) Dynein: A protein with adenosine triphosphatase activity from cilia. *Science* 149:424–426. Available from: https://doi.org/10.1126/science.149.3682.424

13. Gibbons IR (1981) Cilia and flagella of eukaryotes. *J Cell Biol* 91:107s–124s.
Available from: https://doi.org/10.1083/jcb.91.3.107s

14. Manton I, Clarke B, Greenwood AD, Flint EA (1952) Further observations on the structure of plant cilia, by a combination of visual and electron microscopy. *J Exp Bot* 3:204–215. Available from: https://doi.org/10.1093/jxb/3.2.204

15. Hafezparast M, Klocke R, Ruhrberg C, Marquardt A, Ahmad-Annuar A, Bowen S, Lalli G, Witherden AS, Hummerich H, Nicholson S, et al. (2003) Mutations in dynein link motor neuron degeneration to defects in retrograde transport. *Science* 300:808–812.
Available from: https://doi.org/10.1126/science.1083129

16. Imtiaz F, Allam R, Ramzan K, Al-Sayed M (2015) Variation in DNAH1 may contribute to primary ciliary dyskinesia. *BMC Med Genet* 16:14.
Available from: https://doi.org/10.1186/s12881-015-0162-5

17. Toda A, Tanaka H, Kurisu G (2018) Structural atlas of dynein motors at atomic resolution. *Biophys Rev* 10:677–686. Available from: https://doi.org/10.1007/s12551-018-0402-y

18. Stuchell-Brereton MD, Siglin A, Li J, Moore JK, Ahmed S, Williams JC, Cooper JA (2011) Functional interaction between dynein light chain and intermediate chain is required for mitotic spindle positioning. *Mol Biol Cell* 22:2690–2701.
Available from: https://doi.org/10.1091/mbc.e11-01-0075

19. Habura A, Tikhonenko I, Chisholm RL, Koonce MP (1999) Interaction mapping of a dynein heavy chain: Identification of dimerization and intermediate-chain binding domains. *Journal of Biological Chemistry* 274:15447–15453.
Available from: https://doi.org/10.1074/jbc.274.22.15447

20. Asai DJ, Koonce MP (2001) The dynein heavy chain: structure, mechanics and evolution. *Trends Cell Biol* 11:196–202.
Available from: https://doi.org/10.1016/S0962-8924(01)01970-5

21. Tynan SH, Gee MA, Vallee RB (2000) Distinct but overlapping sites within the cytoplasmic dynein heavy chain for dimerization and for intermediate chain and light intermediate chain binding. *Journal of Biological Chemistry* 275:32769–32774.
Available from: https://doi.org/10.1074/jbc.M001537200

22. Schmidt H, Carter AP (2016) Review: Structure and mechanism of the dynein motor ATPase. *Biopolymers* 105:557–567. Available from: https://doi.org/10.1002/bip.22856

23. Carter AP (2013) Crystal clear insights into how the dynein motor moves. *J Cell Sci* 126:705–713. Available from: https://doi.org/10.1242/jcs.120725

24. Goodenough U, Heuser J (1984) Structural comparison of purified dynein proteins with *in situ* dynein arms. *J Mol Biol* 180:1083–1118.
Available from: https://doi.org/10.1016/0022-2836(84)90272-9

25. Nishikawa Y, Inatomi M, Iwasaki H, Kurisu G (2016) Structural change in the dynein stalk

region associated with two different affinities for the microtubule. *J Mol Biol* 428:1886–1896. Available from: https://doi.org/10.1016/j.jmb.2015.11.008

26. Kon T, Imamula K, Roberts AJ, Ohkura R, Knight PJ, Gibbons IR, Burgess SA, Sutoh K (2009) Helix sliding in the stalk coiled coil of dynein couples ATPase and microtubule binding. *Nat Struct Mol Biol* 16:325–333. Available from: https://doi.org/10.1038/nsmb.1555

27. Gibbons IR, Garbarino JE, Tan CE, Reck-Peterson SL, Vale RD, Carter AP (2005) The affinity of the dynein microtubule-binding domain is modulated by the conformation of its coiled-coil stalk. *Journal of Biological Chemistry* 280:23960–23965.
Available from: https://doi.org/10.1074/jbc.M501636200

28. Kato YS, Yagi T, Harris SA, Ohki S, Yura K, Shimizu Y, Honda S, Kamiya R, Burgess SA, Tanokura M (2014) Structure of the microtubule-binding domain of flagellar dynein. *Structure* 22:1628–1638. Available from: https://doi.org/10.1016/j.str.2014.08.021

29. Ben Khelifa M, Coutton C, Zouari R, Karaouzène T, Rendu J, Bidart M, Yassine S, Pierre V, Delaroche J, Hennebicq S, et al. (2014) Mutations in DNAH1, which encodes an inner arm heavy chain dynein, lead to male infertility from multiple morphological abnormalities of the sperm flagella. *The American Journal of Human Genetics* 94:95–104.
Available from: https://doi.org/10.1016/j.ajhg.2013.11.017

30. Toda A, Nishikawa Y, Tanaka H, Yagi T, Kurisu G (2020) The complex of outer-arm dynein light chain-1 and the microtubule-binding domain of the γ heavy chain shows how axonemal dynein tunes ciliary beating. *Journal of Biological Chemistry* 295:3982–3989.
Available from: https://doi.org/10.1074/jbc.RA119.011541

31. Lacey SE, He S, Scheres SHW, Carter AP (2019) Cryo-EM of dynein microtubule-binding domains shows how an axonemal dynein distorts the microtubule. *Elife* 8:e47145.

Available from: https://doi.org/10.7554/eLife.47145

32. Kon T, Oyama T, Shimo-Kon R, Imamula K, Shima T, Sutoh K, Kurisu G (2012) The 2.8 Å crystal structure of the dynein motor domain. *Nature* 484:345–350.
Available from: https://doi.org/10.1038/nature10955

33. Kabsch W (2010) XDS. *Acta Crystallographica Section D* 66:125–132. Available from: https://doi.org/10.1107/S0907444909047337

34. Adams PD, Afonine P V, Bunkóczi G, Chen VB, Davis IW, Echols N, Headd JJ, Hung L-W, Kapral GJ, Grosse-Kunstleve RW, *et al*. (2010) PHENIX: a comprehensive Python-based system for macromolecular structure solution. *Acta Crystallographica Section D* 66:213–221. Available from: https://doi.org/10.1107/S0907444909052925

35. Terwilliger TC, Adams PD, Read RJ, McCoy AJ, Moriarty NW, Grosse-Kunstleve RW, Afonine P V, Zwart PH, Hung L-W (2009) Decision-making in structure solution using Bayesian estimates of map quality: the PHENIX AutoSol wizard. *Acta Crystallographica Section D* 65:582–601. Available from: https://doi.org/10.1107/S0907444909012098

36. Emsley P, Lohkamp B, Scott WG, Cowtan K (2010) Features and development of Coot. *Acta Crystallographica Section D* 66:486–501.
Available from: https://doi.org/10.1107/S0907444910007493

37. Afonine P V, Grosse-Kunstleve RW, Echols N, Headd JJ, Moriarty NW, Mustyakimov M, Terwilliger TC, Urzhumtsev A, Zwart PH, Adams PD (2012) Towards automated crystallographic structure refinement with phenix.refine. *Acta Crystallographica Section D* 68:352–367. Available from: https://doi.org/10.1107/S0907444912001308

38. Headd JJ, Echols N, Afonine P V, Grosse-Kunstleve RW, Chen VB, Moriarty NW, Richardson DC, Richardson JS, Adams PD (2012) Use of knowledge-based restraints in

phenix.refine to improve macromolecular refinement at low resolution. *Acta Crystallographica Section D* 68:381–390. Available from: https://doi.org/10.1107/S0907444911047834

39. Walshaw J, Woolfson DN (2001) SOCKET: a program for identifying and analysing coiled-coil motifs within protein structures. *J Mol Biol* 307:1427–1450.
Available from: https://doi.org/10.1093/bioinformatics/btab631

40. Kumar P, Woolfson DN (2021) Socket2: a program for locating, visualizing and analyzing coiled-coil interfaces in protein structures. *Bioinformatics* 37:4575–4577.
Available from: https://doi.org/10.1093/bioinformatics/btab631

41. Strelkov S V, Burkhard P (2002) Analysis of α-helical coiled coils with the program TWISTER reveals a structural mechanism for stutter compensation. *J Struct Biol* 137:54–64.
Available from: https://doi.org/10.1006/jsbi.2002.4454

42. Girdlestone C, Hayward S (2015) The DynDom3D webserver for the analysis of domain movements in multimeric proteins. *Journal of Computational Biology* 23:21–26.
Available from: https://doi.org/10.1089/cmb.2015.0143

43. Mirdita M, Schütze K, Moriwaki Y, Heo L, Ovchinnikov S, Steinegger M (2022) ColabFold: making protein folding accessible to all. *Nat Methods* 19:679–682.
Available from: https://doi.org/10.1038/s41592-022-01488-1

44. Ashkenazy H, Abadi S, Martz E, Chay O, Mayrose I, Pupko T, Ben-Tal N (2016) ConSurf 2016: An improved methodology to estimate and visualize evolutionary conservation in macromolecules. *Nucleic Acids Res* 44:W344–W350.
Available from: https://doi.org/10.1093/nar/gkw408

45. Walton T, Gui M, Velkova S, Fassad MR, Hirst RA, Haarman E, O'Callaghan C, Bottier M, Burgoyne T, Mitchison HM, et al. (2023) Axonemal structures reveal mechanoregulatory

and disease mechanisms. *Nature* 618:625–633.
Available from: https://doi.org/10.1038/s41586-023-06140-2

46. Lindemann CB (1994) A model of flagellar and ciliary functioning which uses the forces transverse to the axoneme as the regulator of dynein activation. *Cell Motil* 29:141–154. Available from: https://doi.org/10.1002/cm.970290206

47. Bell CW, Gibbons IR (1982) Structure of the dynein-1 outer arm in sea urchin sperm flagella. II. Analysis by proteolytic cleavage. *Journal of Biological Chemistry* 257:516–522. Available from: https://doi.org/10.1016/S0021-9258(19)68394-8

48. Gibbons IR (1995) Dynein family of motor proteins: Present status and future questions. *Cell Motil* 32:136–144. Available from: https://doi.org/10.1002/cm.970320214

49. Carter AP, Garbarino JE, Wilson-Kubalek EM, Shipley WE, Cho C, Milligan RA, Vale RD, Gibbons IR (2008) Structure and functional role of dynein's microtubule-binding domain. *Science* 322:1691–1695. Available from: https://doi.org/10.1126/science.1164424

50. Castoldi M, Popov A V (2003) Purification of brain tubulin through two cycles of polymerization–depolymerization in a high-molarity buffer. *Protein Expr Purif* 32:83–88. Available from: https://doi.org/10.1016/S1046-5928(03)00218-3

51. Gigant B, Wang W, Dreier B, Jiang Q, Pecqueur L, Plückthun A, Wang C, Knossow M (2013) Structure of a kinesin–tubulin complex and implications for kinesin motility. *Nat Struct Mol Biol* 20:1001–1007. Available from: https://doi.org/10.1038/nsmb.2624

52. Ecklund KH, Morisaki T, Lammers LG, Marzo MG, Stasevich TJ, Markus SM (2017) She1 affects dynein through direct interactions with the microtubule and the dynein microtubule-binding domain. *Nat Commun* 8:2151.
Available from: https://doi.org/10.1038/s41467-017-02004-2

List of publication

1. Seolmin Ko, Akiyuki Toda, Hideaki Tanaka, Jian Yu, Genji Kurisu (2023) Crystal structure of the stalk region of axonemal inner-arm dynein-d reveals unique features in the coiled-coil and microtubule-binding domain. *FEBS Letters*, available online ahead of print. Available from: https://doi.org/10.1002/1873-3468.14690